International Journal of Solids and Structures 49 (2012) 1497–1517

Contents lists available at SciVerse ScienceDirect

International Journal of Solids and Structures

journal homepage: www.elsevier.com/locate/ijsolstr

Comparative study of different discrete element models and evaluation of equivalent micromechanical parameters

Jerzy Rojek [a], Carlos Labra [b,*], Okan Su [c], Eugenio Oñate [b]

[a] Institute of Fundamental Technological Research, Polish Academy of Sciences, Warsaw, Poland
[b] International Center for Numerical Methods in Engineering (CIMNE), Technical University of Catalonia, Barcelona, Spain
[c] Department of Mining Engineering & Zonguldak Vocational School, Zonguldak Karaelmas University, Zonguldak, Turkey

ARTICLE INFO

Article history:
Received 31 August 2011
Received in revised form 3 February 2012
Available online 24 March 2012

Keywords:
Discrete element method
Brittle
Compression
Contact
Heterogeneity
Modelling

ABSTRACT

Comparative studies of different discrete element models of a rock-type material are presented. The discrete element formulation employs spherical particles with the cohesive interaction model combining linear elastic behaviour with brittle failure. Numerical studies consisted in simulation of the uniaxial compression test. Two cylindrical specimens with particle size distributions yielding different degree of heterogeneity have been used. Macroscopic response produced by different discrete element models has been compared. The main difference between the compared models consists in the evaluation of micromechanical constitutive parameters. Two approaches are compared. In the first approach, the contact stiffness and strength parameters depend on the local particle size, while in the second approach, global uniform contact parameters are assumed for all the contacting pairs in function of average geometric measures characterizing the particle assembly. The size dependent contact parameters are calculated as functions of geometric parameters characterizing each contacting particle pair. As geometric scaling parameters, the arithmetic and harmonic means, as well as the minimum of the radii of two contacting particles are considered. Two different models with size dependent contact parameters are formulated. The performance of these models is compared with that of the discrete element model with global uniform contact parameters. Equivalence between the models with size dependent and uniform contact parameters has been checked. In search of this equivalence, different methods of evaluation of global uniform parameters have been studied. The contact stiffness has been evaluated in terms of the average radius of the particle assembly or in terms of the averages of the arithmetic and harmonic means of the contact pair radii, the geometric parameters used in the evaluation of the contact stiffness in the size-dependent models. The uniform contact strengths have been determined as functions of the averages of radii squares, squares of arithmetic radii means or squares of minimum radii of the contacting pairs.

For the more homogenous specimen, the models with local size dependent parameters and models with global uniform parameters give similar response. The models with uniform parameters evaluated according to the averages of the geometric parameters used in the evaluation of local parameters ensure better agreement with the respective models with size-dependent parameters than the models with uniform parameters evaluated according to the particle radii. Simulations using the more heterogenous specimen reveal differences between the considered models. There are significant differences in stress–strain curves as well as in the failure pattern. The models with local size-dependent parameters are more sensitive to the change of heterogeneity than the model with global uniform parameters.

1. Introduction

Numerical programs employing the discrete element method (DEM) have achieved a status of a standard analysis tool in geomechanics (Donze et al., 2009). However, it seems that there is a lack of full understanding of many micromechanical mechanisms which are inherent in the DEM and influence macroscopic behaviour of DEM models. In the DEM, a material is represented by an assembly of particles interacting among one another with contact forces. Interparticle interaction models can be based on different types of contact laws incorporating different physical effects such as elasticity, viscosity, damage and friction (Donze et al., 2009; Kruggel-Emden et al., 2008; Luding, 2008; Chang and Hicher, 2005). Constitutive models for rocks must also take into account

* Corresponding author.
E-mail addresses: jrojek@ippt.gov.pl (J. Rojek), clabra@cimne.upc.edu (C. Labra), okansu@karaelmas.edu.tr (O. Su), onate@cimne.upc.edu (E. Oñate).

0020-7683/$ - see front matter © 2012 Elsevier Ltd. All rights reserved.
http://dx.doi.org/10.1016/j.ijsolstr.2012.02.032

cohesive interaction between particles. Even using a simple model such as the linear elastic-perfectly brittle model employed in the present work, a complex behaviour at the macroscopic scale can be obtained. Depending on the set of local parameters a more brittle or more ductile macroscopic behaviour can be obtained (Huang, 1999).

The main difficulty in using the DEM consists in adopting adequate interparticle contact model and appropriate model parameters which yield a required macroscopic behaviour. Many studies have been carried out to investigate the effect of local (microscopic) parameters in the discrete element method on macroscopic mechanical properties (Hsieh et al., 2008; Cambou et al., 2000; Kruyt and Rothenburg, 2004). The contact stiffness and bond strength are usually taken as the most significant parameters influencing precritical behaviour and failure of rock materials (Hsieh et al., 2008; Fakhimi and Villegas, 2007; Potyondy and Cundall, 2004). Friction coefficient, which is an important factor in granular materials, has small influence on the peak strength in the discrete element models of rock materials (Fakhimi and Villegas, 2007). Following these findings, our attention in this work will also be concentrated on the effect of the contact stiffness and strength parameters.

The main purpose of the present work is to study the influence of the evaluation method of local stiffness and strength parameters in the discrete element method on the macroscopic properties and macroscopic behaviour of the material model. Two approaches are compared. In the first approach, the stiffness and strength parameters of the contact model are assumed to depend on the size of contacting particles and are evaluated locally as certain functions of contacting pair radii (Potyondy and Cundall, 2004; PFC^{3D}, 2006). In the second approach, uniform microscopic properties are assumed in the whole discrete element assembly (Rojek et al., 2001, 2008; Kruyt and Rothenburg, 2004; Tavarez and Plesha, 2007). The values of the global microscopic parameters can be evaluated taking into account some average particle size measure for the whole discrete element model (Agnolin and Roux, 2008; Huang and Detournay, 2008; Tavarez and Plesha, 2007).

There are no works showing the effect of the evaluation of local parameters on macroscopic behaviour. The present work is intended to fill this gap. The discrete element models, which will be studied, have been implemented in the discrete element program DEMPack (CIMNE, 2010). The numerical studies will consist in simulation of the the unconfined compressive strength (UCS) test of a rock-type material. The UCS test, which is used in engineering practice as a standard test to determine mechanical properties of rocks (Price et al., 1994), is also commonly used in calibration of discrete element models (D'Addetta et al., 2002; Fakhimi and Villegas, 2007; Rojek et al., 2011; Ng, 2006; Huang, 1999; Potyondy and Cundall, 2004; Huang and Detournay, 2008). The results obtained in our simulations using different discrete element models will be compared with one another. The mechanical response characterized by strength and elastic parameters as well as by failure type will be investigated in order to determine similarities and differences between the studied models.

The comparative studies presented in this work involve different possibilities to calculate size dependent local stiffness and strength parameters. Macroscopic behaviour obtained for different local size scaling parameter is compared. Then, a possible equivalence of these models and the model with uniform parameters will be investigated. Different options to determine global parameters equivalent to local size dependent parameters will be tested. It will be investigated how strongly the method of evaluation of local parameters affects macroscopic behaviour in the discrete element model.

Rocks are heterogenous materials and their macroscopic properties are strongly influenced by their heterogeneity at microscale (Blair and Cook, 1998). As is explained by Blair and Cook (1998), increasing geometric heterogeneity in a material increases the number and magnitude of local stress concentrations. Crack formation, growth and coalescence in more heterogenous material occur at lower average stress levels. Within the discrete element method, random packing of non-uniform size particles gives a non-homogenous geometric model. Packing and size distribution of discrete elements greatly contribute to non-uniform distribution of the interaction forces and their intensities, and in consequence influence the failure mode (Boutt and McPherson, 2002; Voivret et al., 2009; Antonellini and Pollard, 1995; Madadi et al., 2004). The effect of particle packing and size distribution will be studied by comparing the results obtained using two specimens characterized by different particle packing and size distribution.

The heterogeneity of the discrete element material model can be further contributed by the spatial distribution of local model parameters, which can result from the method of evaluation of discrete element parameters. In order to check this effect in the present work much attention will be paid to the distributions of the geometric parameters used in evaluation of the contact stiffness and strength.

2. Discrete element method formulation

2.1. Basic assumptions

Within the discrete element method (DEM), it is assumed that a material can be represented by an assembly of rigid particles interacting with one another. In general, the shape of the particles can be arbitrary, in this work spherical elements are employed. A discrete element formulation using spherical or cylindrical particles was first proposed by Cundall and Strack (1979) and Cundall (1988a,b). A similar formulation has been developed and implemented in the discrete and finite element code DEMPack (Rojek and Oñate, 2004; Oñate and Rojek, 2004; CIMNE, 2010). Simulation results presented in this work have been obtained using the DEMpack program.

2.2. Equations of motion

The translational and rotational motion of discrete elements (particles) is described by means of the Newton–Euler equations of rigid body dynamics. For the ith element we have

$$m_i\ddot{\mathbf{u}}_i = \mathbf{F}_i \tag{1}$$

$$J_i\dot{\boldsymbol{\omega}}_i = \mathbf{T}_i \tag{2}$$

where $\mathbf{u}_i$ is the element centroid displacement in a fixed (inertial) coordinate frame $\mathbf{X}$, $\boldsymbol{\omega}_i$ – the angular velocity, m_i – the element mass, J_i – the moment of inertia, $\mathbf{F}_i$ – the resultant force, and $\mathbf{T}_i$ – the resultant moment about the central axes. The form of the rotational Eq. (2), which is valid for spheres, is simplified with respect to a general form for an arbitrary rigid body with the rotational inertial properties represented by a second order tensor. Vectors $\mathbf{F}_i$ and $\mathbf{T}_i$ are sums of: (i) all forces and moments applied to the ith element due to external load, $\mathbf{F}_i^{\text{ext}}$ and $\mathbf{T}_i^{\text{ext}}$, respectively, (ii) contact interactions with neighbouring spheres $\mathbf{F}_{ij}^{\text{cont}}$, $j = 1,\ldots,n_i^c$, where n_i^c is the number of elements being in contact with the ith discrete element, (iii) forces and moments resulting from external damping, $\mathbf{F}_i^{\text{damp}}$ and $\mathbf{T}_i^{\text{damp}}$, respectively, which can be written as:

$$\mathbf{F}_i = \mathbf{F}_i^{\text{ext}} + \sum_{j=1}^{n_i^c}\mathbf{F}_{ij}^{\text{cont}} + \mathbf{F}_i^{\text{damp}} \tag{3}$$

$$\mathbf{T}_i = \mathbf{T}_i^{\text{ext}} + \sum_{j=1}^{n_i^c}\mathbf{l}_{ij}^{c} \times \mathbf{F}_{ij}^{\text{cont}} + \mathbf{T}_i^{\text{damp}} \tag{4}$$

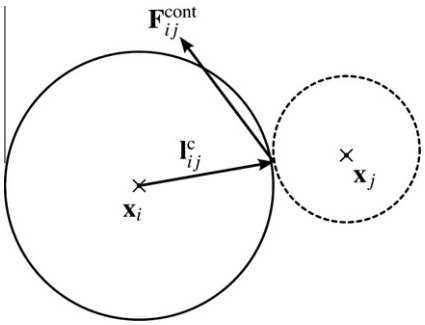

Fig. 1. Contact interaction between two discrete elements.

where $\mathbf{l}_{ij}^{\text{c}}$ is the vector connecting the centre of mass of the ith element with the contact point with the jth element (Fig. 1).

Similarly as in PFC^{3D} (2006), the damping terms $\mathbf{F}_i^{\text{damp}}$ and $\mathbf{T}_i^{\text{damp}}$ in Eqs. (3) and (4) in the present work are of non-viscous type and are given by:

$$\mathbf{F}_i^{\text{damp}} = -\alpha^t \left\| \mathbf{F}_i^{\text{ext}} + \sum_{j=1}^{n_i^c} \mathbf{F}_{ij}^{\text{cont}} \right\| \frac{\dot{\mathbf{u}}_i}{\|\dot{\mathbf{u}}_i\|} \tag{5}$$

$$\mathbf{T}_i^{\text{damp}} = -\alpha^r \left\| \mathbf{T}_i^{\text{ext}} + \sum_{j=1}^{n_i^c} \mathbf{l}_{ij}^{\text{c}} \times \mathbf{F}_{ij}^{\text{cont}} \right\| \frac{\boldsymbol{\omega}_i}{\|\boldsymbol{\omega}_i\|} \tag{6}$$

where α^t and α^r, are respective damping factors for translational and rotational motion.

2.3. Constitutive contact models

The overall behaviour of the system is determined by the contact laws assumed for the particle interaction. The contact law can be seen as the formulation of the material model on the microscopic level. Contact models in the discrete element method can include force and moment interaction between particles. In the present work, contact moments are not considered.

Formulation of the constitutive model employs the decomposition of the contact force between two elements[1] $\mathbf{F}^{\text{cont}}$ into normal and tangential components, $\mathbf{F}_n$ and $\mathbf{F}_s$, respectively:

$$\mathbf{F}^{\text{cont}} = \mathbf{F}_n + \mathbf{F}_s = F_n\mathbf{n} + \mathbf{F}_s \tag{7}$$

where $\mathbf{n}$ is the unit vector along the line connecting the centroids of two contacting particles. Modelling of rock or other cohesive materials requires contact models with cohesion allowing tensile interaction force between particles (Potyondy and Cundall, 2004; Choi, 1992; Rojek et al., 2001). In the present formulation, rock materials are modelled using the elastic-perfectly brittle model of contact interaction, in which initial bonding between neighbouring particles is assumed. These bonds can be broken under excessive load which allows us to simulate initiation and propagation of material fracture. Contact laws for the normal and tangential direction in the elastic-perfectly brittle model are shown in Fig. 2. When two particles are bonded the contact forces in both normal and tangential directions are calculated from the linear constitutive relationships:

$$F_n = K_n u_n \tag{8}$$

$$\|\mathbf{F}_s\| = K_s \|\mathbf{u}_s\| \tag{9}$$

where K_n – interface stiffness in the normal direction, K_s – interface stiffness in the tangential direction, u_n – overlap ($u_n \leqslant 0$) or gap ($u_n > 0$) at the contact point, $\mathbf{u}_s$ – relative displacement at the contact point in tangential direction. Consistently with the sign convention for u_n and Eq. (8), the normal force F_n is negative in compression and positive in tension. The particle gap/penetration u_n is given in terms of the distance between the particle centroids d and their radii r_i and r_j

$$u_n = d - r_i - r_j \tag{10}$$

and the relative tangential displacement $\mathbf{u}_s$ is updated incrementally

$$\mathbf{u}_s = \mathbf{u}_s^{\text{old}} + \Delta\mathbf{u}_s \tag{11}$$

where $\mathbf{u}_s^{\text{old}}$ is the vector of the relative tangential displacement from the previous time step rotated to the present contact plane and $\Delta\mathbf{u}_s$ is the incremental relative tangential displacement

$$\Delta\mathbf{u}_s = \mathbf{v}_s \Delta t \tag{12}$$

with $\mathbf{v}_s$ being the relative tangential velocity at the contact point determined as

$$\mathbf{v}_s = \mathbf{v}_{\text{r}}^{\text{c}} - (\mathbf{v}_{\text{r}}^{\text{c}} \cdot \mathbf{n})\mathbf{n} \tag{13}$$

where $\mathbf{v}_{\text{r}}^{\text{c}}$ is the relative velocity at the contact point

$$\mathbf{v}_{\text{r}}^{\text{c}} = \left(\dot{\mathbf{u}}_j + \boldsymbol{\omega}_j \times \mathbf{l}_{ji}^{\text{c}}\right) - \left(\dot{\mathbf{u}}_i + \boldsymbol{\omega}_i \times \mathbf{l}_{ij}^{\text{c}}\right) \tag{14}$$

Cohesive bonds are broken instantaneously when the interface strength is exceeded in the tangential direction by the tangential contact force or in the normal direction by the tensile contact force

$$F_n \geqslant \phi_n \tag{15}$$

$$\|\mathbf{F}_s\| \geqslant \phi_s \tag{16}$$

where ϕextsubscript$n$ – interface strength in the normal direction, ϕ_s – interface strength in the tangential direction. After decohesion, the contact is treated assuming a standard contact model with Coulomb friction. The normal contact force can be compressive only ($F_n \leqslant 0$) and the tangential contact force is limited by $\mu|F_n|$

$$\|\mathbf{F}_s\| \leqslant \mu|F_n| \tag{17}$$

where μ is the Coulomb friction coefficient.

Although the constitutive model adopted in this work is relatively simple, numerical tests show that a macroscopic behaviour of brittle rocks is represented properly. The deformation behaviour of brittle rocks under uniaxial compression before fracture is predominantly linear and can be modelled correctly with the linear elastic microscopic law. The perfectly brittle fracture criterion, employed in the microscopic model, reproduces well a brittle failure of rocks. A known drawback associated with the failure criterion defined by the Eqs. (15) and (16) is the difficulty with reproducing a failure envelope for different confining pressures. Potyondy and Cundall (2004) have shown, that the angle of internal friction obtained using this type of failure criterion is smaller than the values characterizing hard rocks. Employing a pressure dependent failure criterion for the shear force (Hentz et al., 2004) allowed Wang and Tonon (2009) to obtain appropriate failure envelope for granite. In our work, we will investigate unconfined compression strength of the rock material only. For this purpose, the model adopted is sufficiently accurate.

3. Evaluation of stiffness and strength parameters of the contact models

The constitutive contact model presented in Section 2.3 is defined by the following set of parameters:

- Stiffness parameters, K_n and K_s.
- Strength parameters, ϕ_n and ϕ_s.
- Coulomb friction coefficient μ.

[1] In the next part of this section indices denoting the elements will be omitted.

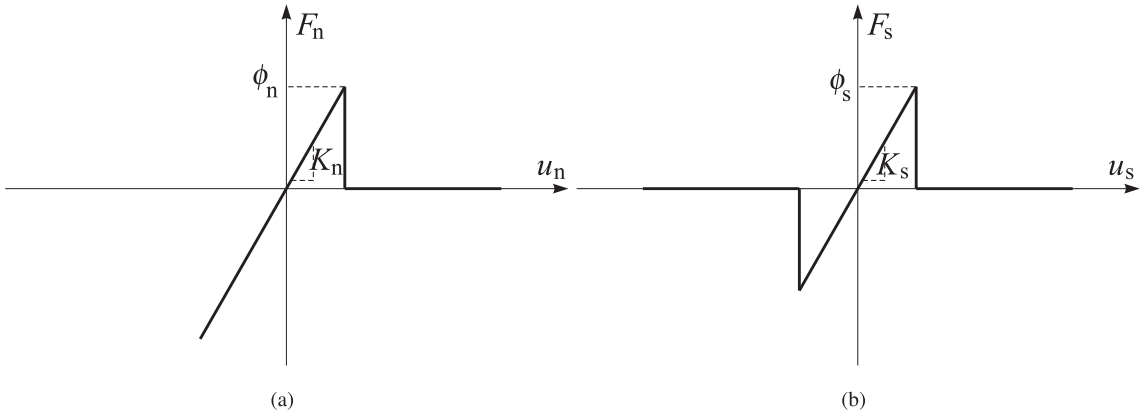

Fig. 2. Force–displacement relationships for the elastic-perfectly brittle model: (a) in the normal direction, (b) in the tangential direction (for the tensile normal force).

The formulation presented in Section 2.3 is employed in all the discrete element models which are studied in this work. The main difference between the compared models consists in the evaluation of the stiffness and strength parameters, K_n, K_s, ϕ_n and ϕ_s. Basically, we can distinguish two approaches in evaluation of these parameters. In the first approach the parameters K_n, K_s, ϕ_n and ϕ_s are taken as uniform in the whole discrete element assembly (Rojek et al., 2001; Rojek et al., 2008). The same value of these parameters is assumed for all the contacting pairs of particles. In the other approach, these parameters are calculated locally, usually assuming that they depend on the contacting particle size (Potyondy and Cundall, 2004) and can be given by certain functions of the particle radii r_i and r_j:

$$K_n = f_{K_n}(r_i, r_j), \quad K_s = f_{K_s}(r_i, r_j), \quad \phi_n = f_{\phi_n}(r_i, r_j), \quad \phi_s = f_{\phi_s}(r_i, r_j) \tag{18}$$

It is worth noting that varying local properties can also be obtained by introducing a spatial randomness of the parameters (Herrmann and Roux, 1990), but in the present work, this type of randomness is not considered.

There may be different assumptions about the form of the functions $f_{K_n}(r_i, r_j)$, $f_{K_s}(r_i, r_j)$, $f_{\phi_n}(r_i, r_j)$ and $f_{\phi_s}(r_i, r_j)$. In this work, two different models using particle size dependent stiffness and strength parameters are studied. The third model employs global uniform constitutive parameters. The performance of the models with locally scaled and global uniform parameters will be compared, investigating possible equivalence and differences. Different methodologies to estimate equivalent parameters for the models employing the size dependent parameters and the model using the uniform parameters will be studied.

3.1. Stiffness and strength parameters in model 1

Cohesive bonding between two particles can be treated as a bar of length L and uniform cross-sectional area A (Potyondy and Cundall, 2004). The schematic connection of a pair of particles by means of a bar is shown in Fig. 3.

The axial force in a bar can be calculated from the following formula:

$$F_n = \frac{E_c A}{L} u_n \tag{19}$$

where E_c is the Young's modulus of the bar material. Taking the length

$$L = r_i + r_j = 2\bar{r} \tag{20}$$

and the area

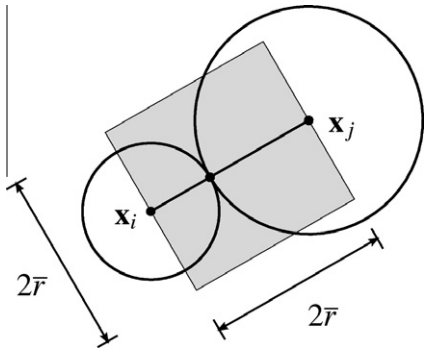

Fig. 3. Schematic connection of two particles in the model 1.

$$A = (2\bar{r})^2 \tag{21}$$

where r_i and r_j are the radii of the two contacting particles, $\bar{r}$ is their arithmetic mean

$$\bar{r} = \frac{r_i + r_j}{2} \tag{22}$$

and substituting the above values into Eq. (19) we obtain

$$F_n = 2E_c\bar{r}u_n \tag{23}$$

Comparing Eqs. (23) and (8) we can see that the stiffness modulus K_n is given by the following expression:

$$K_n = 2E_c\bar{r} \tag{24}$$

In general, the parameter E_c cannot be identified with the Young's modulus of an equivalent continuum material E. With the above assumptions, these two parameters are equivalent for a regular cubic packing of equal particles, only. For an arbitrary packing of particles the contact stiffness modulus E_c is a certain scaling constant correlated with the Young's modulus of equivalent continuum material E. It is strongly dependent on the density of contact connections between particles. The shear stiffness of a bond between two particles K_s is computed assuming a certain value for the ratio of the normal and shear stiffness (K_n/K_s).

Assuming maximum tensile and shear stresses in the bar connecting a pair of particles, σ_c and τ_c, the respective strengths of the bond, ϕ_n and ϕ_s, can be expressed in the following form:

$$\phi_n = \sigma_c A = \sigma_c(2\bar{r})^2 = 4\sigma_c\bar{r}^2 \tag{25}$$

$$\phi_s = \sigma_s A = \tau_c(2\bar{r})^2 = 4\tau_c\bar{r}^2 \tag{26}$$

Eqs. (24)–(26) show that the stiffness and strength parameters of the discrete element model evaluated locally are functions of the mean arithmetic radius of two contacting particles.

3.2. Stiffness and strength parameters in model 2

In this model, the cohesive bond connecting two particles of radii r_i and r_j is treated as a bar of non-uniform cross-sectional area (Fig. 4), consisting of two segments, each having the cross-sectional area and length proportional to the particle size

$$L = L_i + L_j \tag{27}$$

$$L_i = r_i, \quad L_j = r_j \tag{28}$$

$$A_i = (2r_i)^2, \quad A_j = (2r_j)^2 \tag{29}$$

The system of the two bar segments can be treated as two springs connected in series. The axial force F_n transferred by the whole system is equal to the forces in the segments i and j, F_n^i and F_n^j:

$$F_n = F_n^i = F_n^j \tag{30}$$

The overall axial deformation of the system u_n is composed of the deformations of both segments, u_n^i and u_n^j

$$u_n = u_n^i + u_n^j \tag{31}$$

The force–displacement relationships for the whole system and for each bar can be written in the following form:

$$F_n = K_n u_n \tag{32}$$

$$F_n^i = k_n^i u_n^i \tag{33}$$

$$F_n^j = k_n^j u_n^j \tag{34}$$

where K_n is the equivalent stiffness of the system of two bar segments, and k_n^i and k_n^j are stiffnesses of the segments i and j. Substituting Eqs. (31)–(33) into Eq. (31) and taking into account Eq. (30) we obtain the following equation for the stiffness K_n:

$$\frac{1}{K_n} = \frac{1}{k_n^i} + \frac{1}{k_n^j} \tag{35}$$

which can be transformed to the form

$$K_n = \frac{k_n^i k_n^j}{k_n^i + k_n^j} \tag{36}$$

Expression (36) is identical to that used by Potyondy and Cundall (2004) to evaluate the contact stiffness. However, the physical interpretation of the formula (36) was not given there.

Using the assumptions (28) and (29) the stiffness of the segments i and j can be expressed as follows:

$$k_n^i = \frac{E_c^i A^i}{L_i} = 4E_c^i r_i \tag{37}$$

$$k_n^j = \frac{E_c^j A^j}{L_j} = 4E_c^j r_j \tag{38}$$

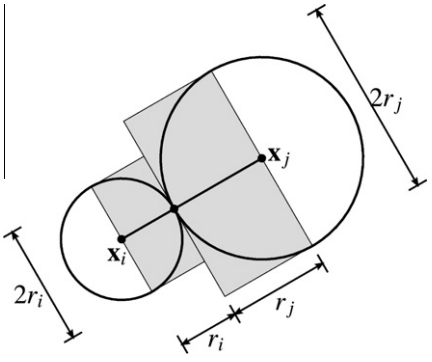

Fig. 4. Schematic connection of two particles in the model 2.

where E_c^i and E_c^j are the Young's moduli of the materials of the segments i and j of the bar. Introducing the relationships (37) and (38) into the formula (36) and assuming that the stiffness moduli E_c^i and E_c^j are equal, we obtain the expression for the equivalent stiffness K_n in the following form:

$$K_n = 4E_c \frac{r_i r_j}{r_i + r_j} \tag{39}$$

It can be noticed that using the harmonic mean $\tilde{r}$ of the radii r_i and r_j

$$\tilde{r} = \frac{2r_i r_j}{r_i + r_j} \tag{40}$$

the formula (39) can be written in the form

$$K_n = 2E_c \tilde{r} \tag{41}$$

analogical to Eq. (24) obtained in model 1. The difference consists in using the harmonic mean instead of the arithmetic one. Except for the case of equal particles, the harmonic mean is always smaller than the arithmetic mean so the overall stiffness of the discrete element model 2 should always be smaller than the stiffness of the discrete element model 1 when both models are applied to the same discrete element geometrical model.

Similarly as in model 1, the equivalent shear stiffness of the bond, K_s in model 2 is computed by using the ratio of the normal and shear stiffness (K_n/K_s). The normal and shear strengths of the bond, ϕ_n and ϕ_s, are given in terms of the maximum tensile and shear stresses, σ_c and τ_c, and a certain geometrical parameter. In this model, consistently with the geometrical assumption for the connecting bar, the strength is limited by the cross-section area of the smaller segment, A_m:

$$\phi_n = \sigma_c A_m = \sigma_c (2r_m)^2 = 4\sigma_c r_m^2 \tag{42}$$

$$\phi_s = \sigma_s A_m = \tau_c (2r_m)^2 = 4\tau_c r_m^2 \tag{43}$$

where

$$r_m = \min(r_i, r_j) \tag{44}$$

Choosing the minimum of the radii in Eq. (44) as a scaling parameter for the strength calculations in Eqs. (42) and (43) may be looked upon as an analogy to the Weibull weakest link model employed in the fracture analysis of brittle materials (Munkholm and Perfect, 2005; Bažant et al., 2004). The weakest link concept postulates that the failure load is governed by the statistically weakest point in the structure. Within the framework of the discrete element method, a similar assumption to that expressed by Eq. (44), has been adopted by Potyondy and Cundall to determine the maximum force transmitted by the cohesive parallel bond (Potyondy and Cundall, 2004).

3.3. Stiffness and strength parameters in model 3

In contrast to the models 1 and 2, the contact parameters in the model 3 are set equal for all the bonds (Rojek et al., 2001; Oñate and Rojek, 2004). This approach has certain advantages since it allows us to find analytical relationship between micro- and macroscopic constitutive parameters (Liao et al., 1997; Liao and Chan, 1997).

The contact stiffness K_n is prescribed directly in this model. This corresponds to the assumption that we prescribe the stiffness of a spring connecting two particles. Except for K_n, the ratio K_n/K_s and the normal and shear bond strengths, ϕ_n and ϕ_s, are assumed constant for all the contacting pairs and are given as input data in this model. The influence of the particle size on the value of these parameters can be taken into account globally, for instance, by considering an average particle size in the evaluation of the model parameters.

An advantage of such an approach consisting in the possibility to use analytical averaging procedures in the evaluation of the model parameters has already been mentioned above. This model may produce mechanical behaviour which is different from those obtained with the local size dependent parameters. This will be shown later in this paper.

4. Determination of equivalent model parameters

The models 1 and 2, in which contact parameters are evaluated locally according to the contacting particle size are defined by the following set of parameters: the contact Young's modulus E_c, the ratio of the shear and normal stiffness K_n/K_s, normal and shear strength parameters, σ_c and τ_c, respectively. It can be noticed that the same parameters are used in the two considered models.

The set of parameters required to define the contact connection in model 3 consists of the following parameters: the normal contact stiffness K_n, the ratio of normal and shear stiffness K_n/K_s, and the normal and shear bond strengths, ϕ_n and ϕ_s, respectively.

The sets of the contact parameters in all the four models are completed with the inter-particle friction coefficient μ as well as adequate damping coefficients, α^t and α^r.

Comparative studies of the formulations employing locally evaluated and global uniform parameters will require equivalent contact model parameters ensuring similar macroscopic properties. Having assumed the contact parameters for the models 1 and 2, the parameters for the model 3 will be determined adapting the formulae for the models 1 and 2 by the use of appropriate average measures obtained for the whole assembly instead of the radii of individual particle pairs.

Using the average of the radii of all the particles in the specimen $\langle r \rangle$ in Eq. (24) instead of $\bar{r}$, or in Eq. (41) instead of $\tilde{r}$, the equivalent normal contact stiffness in the model 3 is obtained in the following form:

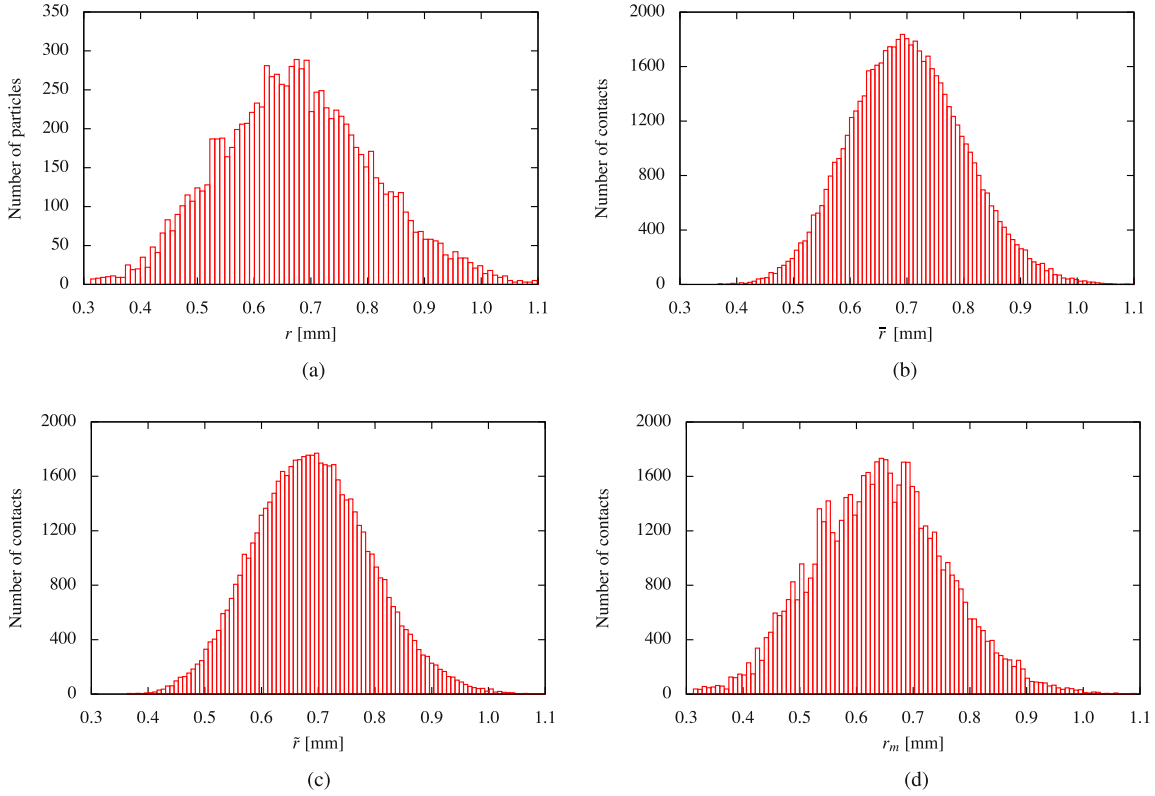

Fig. 5. Distribution of the characteristic geometric parameters for the specimen 1: (a) distribution of the particle radii, (b) distribution of the arithmetic means $\bar{r}$ of the radii of the contacting particle pairs, (c) distribution of the harmonic means $\tilde{r}$ of the radii of the contacting particle pairs, (d) distribution of the minimum radii of the contacting particles r_m.

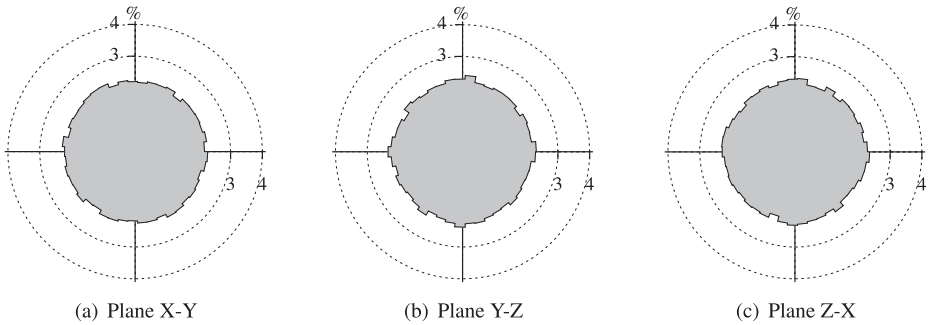

Fig. 6. Polar distribution of contact directions for the specimen 1.

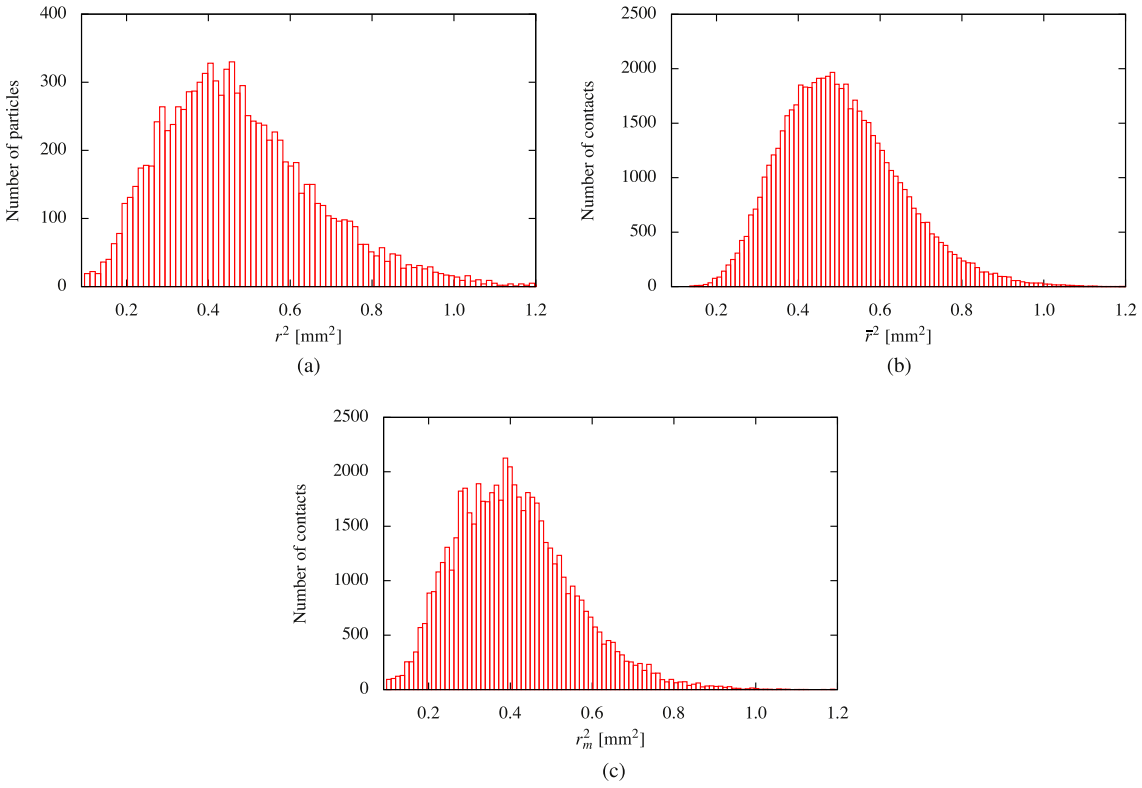

Fig. 7. Distribution of the squares of the characteristic geometric parameters for the specimen 1: (a) distribution of the particle radius squares r^2, (b) distribution of the squares of the arithmetic means of the contacting particle radii $\bar{r}^2$, (c) distribution of the squares of the minimum radii of the contacting particles r_m^2.

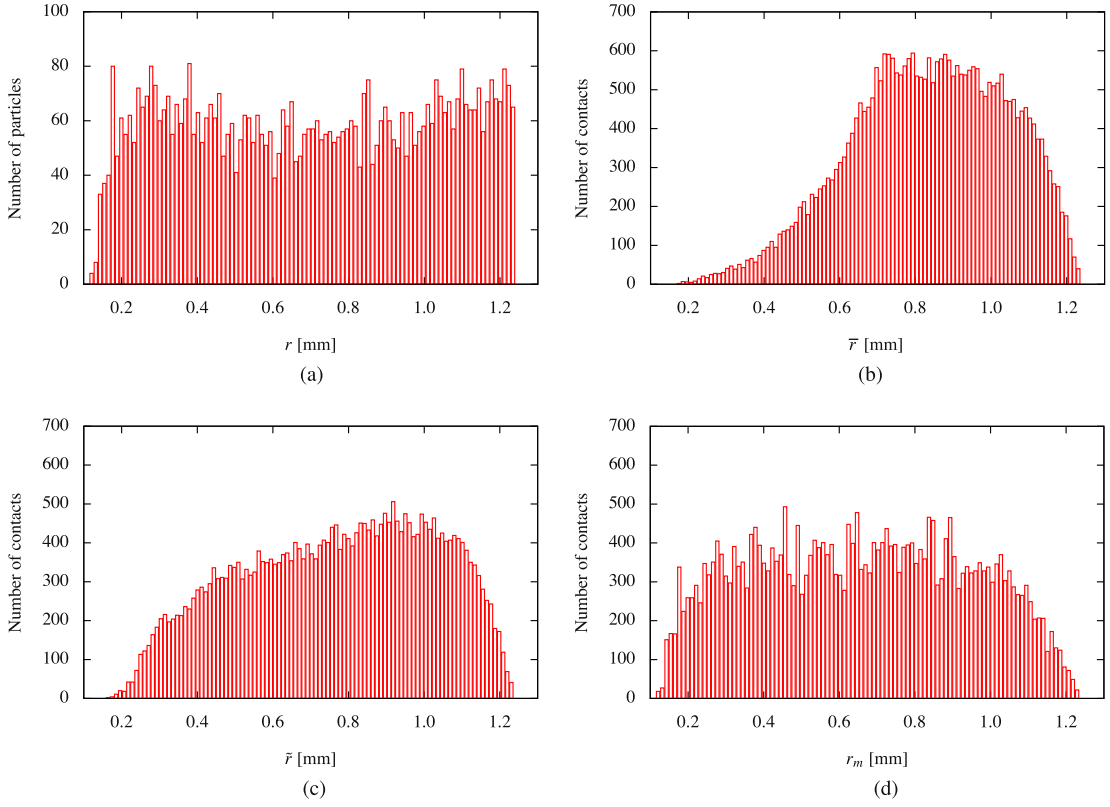

Fig. 8. Distribution of the characteristic geometric parameters for the specimen 2: (a) distribution of the particle radii, (b) distribution of the arithmetic means of the radii of the contacting particle pairs $\bar{r}$, (c) distribution of the harmonic means of the radii of the contacting particle pairs $\tilde{r}$, (d) distribution of the minimum radii of the contacting particles r_m.

$$K_n = 2E_c\langle r\rangle \tag{45}$$

The average radius is calculated considering all the particles in the assembly by

$$\langle r\rangle = \frac{1}{N_p}\sum_{i=1}^{N_p} r_i \tag{46}$$

where N_p is the total number of particles. The equivalent shear stiffness K_s in model 3 can be calculated in a straightforward way assuming the ratio K_n/K_s equal to the ratio K_n/K_s taken in models 1 and 2.

Similarly to the stiffness calculation procedure, the normal and shear strengths for the model are calculated using the averaging procedure, but in this case the average of the squares of the radii is used in the respective formulae

$$\phi_n = 4\sigma_c\langle r^2\rangle \tag{47}$$

$$\phi_s = 4\tau_c\langle r^2\rangle \tag{48}$$

where $\langle r^2\rangle$ is the average of radii squares, given by

$$\langle r^2\rangle = \frac{1}{N_p}\sum_{i=1}^{N_p} r_i^2 \tag{49}$$

The average radius $\langle r\rangle$ and the average of radii squares $\langle r^2\rangle$ do not contain information about contacting pairs in the assembly. A bet-

Table 1
Microscopic parameters of the models 1 and 2 for both specimens.

Parameter	Description	Value
ρ	Density (kg/m^3)	2650
E_c	Young's modulus of the bar material (GPa)	10.0
K_n/K_s	Particle stiffness ratio	3.7
μ	Particle friction coefficient	0.50
σ_c	Contact bond normal strength (MPa)	40
τ_c	Contact bond shear strength (MPa)	40
α^t, α^r	Damping factors	0.7

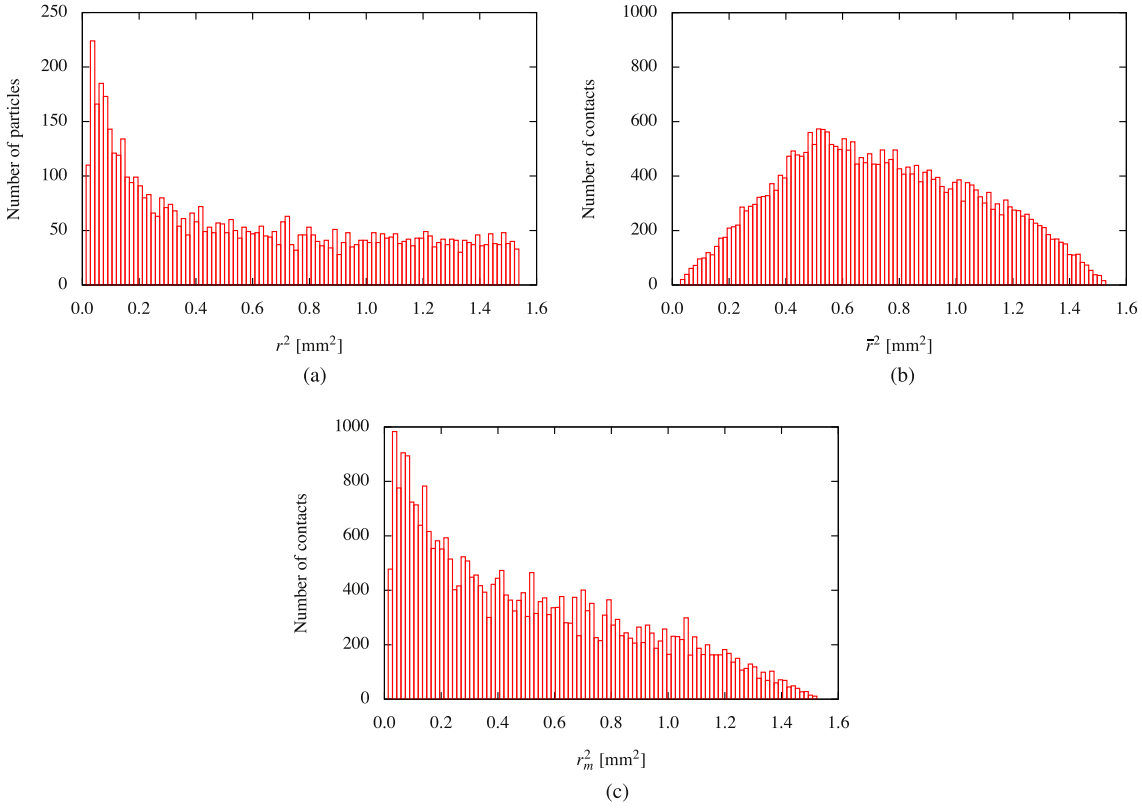

Fig. 9. Distribution of the squares of the characteristic geometric parameters for the specimen 2: (a) distribution of the particle radius squares r^2, (b) distribution of the squares of the arithmetic means of the contacting particle radii $\bar{r}^2$, (c) distribution of the squares of the minimum radii of the contacting particles r_m^2.

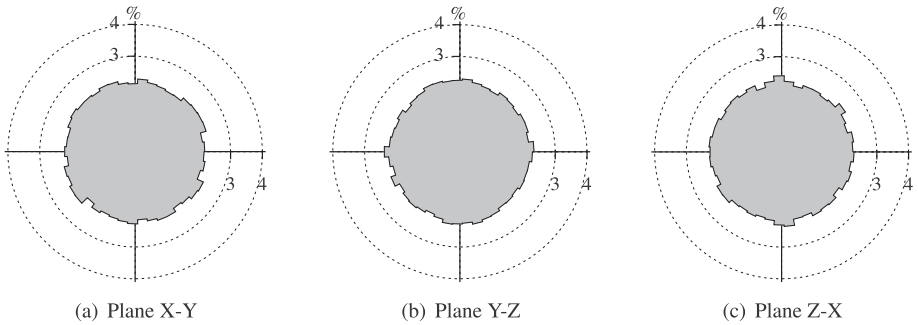

Fig. 10. Polar distribution of contact directions for the specimen 2.

Table 2
Microscopic parameters of the model 3 for the specimen 1.

Parameter	Description	Model 3a	Model 3b	Model 3c
ρ	Density (kg/m^3)	2650	2650	2650
K_n	Contact bond normal stiffness (formula)	$2E_c\langle r\rangle$	$2E_c\langle \bar{r}\rangle$	$2E_c\langle \bar{r}\rangle$
K_n	Contact bond normal stiffness (MN/m)	13.519	14.064	13.819
K_n/K_s	Particle stiffness ratio	3.7	3.7	3.7
μ	Particle friction coefficient	0.50	0.50	0.50
ϕ_n	Contact bond normal strength (formula)	$4\sigma_c\langle r^2\rangle$	$4\sigma_c\langle \bar{r}^2\rangle$	$4\sigma_c\langle r_m^2\rangle$
ϕ_n	Contact bond normal strength (N)	76.001	80.733	65.296
ϕ_s	Contact bond shear strength (N)	76.001	80.733	65.296

Table 3
Microscopic parameters of the model 3 for the specimen 2.

Parameter	Description	Model 3a	Model 3b	Model 3c
ρ	Density (kg/m^3)	2650	2650	2650
K_n	Contact bond normal stiffness (formula)	$2E_c\langle r\rangle$	$2E_c\langle \bar{r}\rangle$	$2E_c\langle \bar{r}\rangle$
K_n	Contact bond normal stiffness (MN/m)	13.987	16.676	15.328
K_n/K_s	Particle stiffness ratio	3.7	3.7	3.7
μ	Particle friction coefficient	0.50	0.50	0.50
ϕ_n	Contact bond normal strength (formula)	$4\sigma_c\langle r^2\rangle$	$4\sigma_c\langle \bar{r}^2\rangle$	$4\sigma_c\langle r_m^2\rangle$
ϕ_n	Contact bond normal strength (N)	95.170	117.99	81.447
ϕ_s	Contact bond shear strength (N)	95.170	117.99	81.447

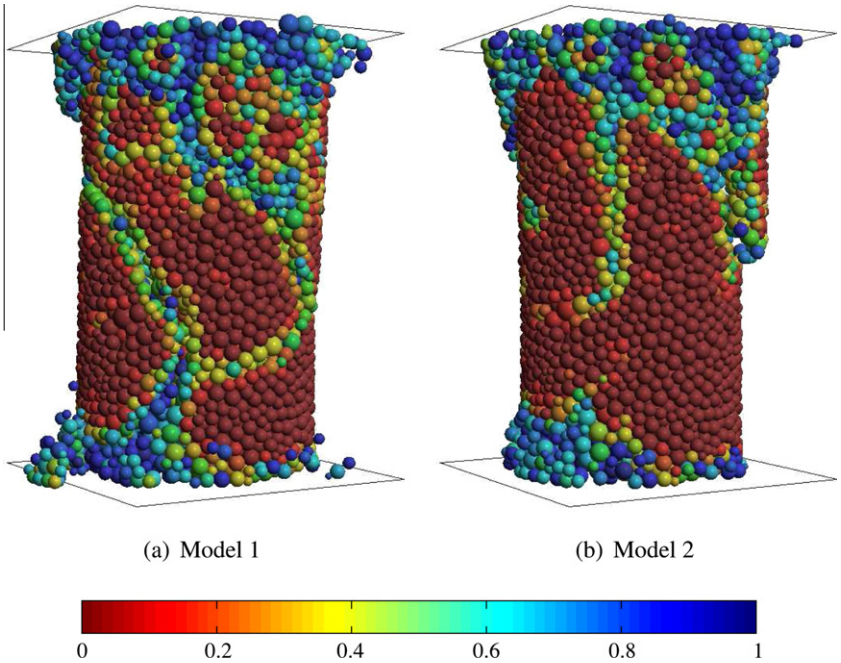

Fig. 11. Damage in the models with local evaluation of the parameters – simulation results for the specimen 1.

ter equivalence can be expected if instead of the average radius $\langle r\rangle$ we take appropriate averages of arithmetic or harmonic means of all the contact pairs in the assembly

$$\langle \bar{r}\rangle = \frac{1}{N_c}\sum_{i=1}^{N_c}\bar{r}_i \tag{50}$$

$$\langle \tilde{r}\rangle = \frac{1}{N_c}\sum_{i=1}^{N_c}\tilde{r}_i \tag{51}$$

where N_c is the total number of contact pairs in the assembly, $\bar{r}_i$ is the arithmetic mean and $\tilde{r}_i$ is the harmonic mean of the radii in the ith contact pair.

Using the average of arithmetic means $\langle \bar{r}\rangle$ in Eq. (24) instead of $\bar{r}$, the normal contact stiffness in the model 3 equivalent to the stiffness of the model 1 is obtained

$$K_n = 2E_c\langle \bar{r}\rangle \tag{52}$$

Analogously, using the average of harmonic means $\langle \tilde{r}\rangle$ in Eq. (41) instead of $\tilde{r}$, the equivalent normal contact stiffness in the model 3 equivalent to the stiffness of the model 2 is obtained

$$K_n = 2E_c\langle \tilde{r}\rangle \tag{53}$$

Equivalent normal and shear strengths will be calculated using respective averages, the average of squares of arithmetic means,

$$\langle \bar{r}^2 \rangle = \frac{1}{N_c} \sum_{i=1}^{N_c} \bar{r}_i^2 \tag{54}$$

or the average of squares of minimum radii

$$\langle r_m^2 \rangle = \frac{1}{N_c} \sum_{i=1}^{N_c} r_{m_i}^2 \tag{55}$$

Using the average of squares of arithmetic means in Eqs. (25) and (26) we obtain the strengths equivalent to the model 1

$$\phi_n = 4\sigma_c \langle \bar{r}^2 \rangle \tag{56}$$

$$\phi_s = 4\tau_c \langle \bar{r}^2 \rangle \tag{57}$$

Using the average of squares of minimum radii in Eqs. (42) and (43) we obtain the strengths equivalent to the model 2

$$\phi_n = 4\sigma_c \langle r_m^2 \rangle \tag{58}$$

$$\phi_s = 4\tau_c \langle r_m^2 \rangle \tag{59}$$

Taking as a criterion different assumptions in calculation of the global uniform parameters we will distinguish the following cases within the model 3:

(a) The normal contact stiffness is calculated according to Eq. (45), and the contact strengths are calculated according to Eqs. (47) and (48). Equivalence with all the other models will be checked.
(b) The normal contact stiffness is calculated according to Eq. (52), and the contact strengths are calculated according to Eqs. (56) and (57). Equivalence with the model 1 is assumed and will be checked.
(c) The normal contact stiffness is calculated according to Eq. (53), and the contact strengths are calculated according to Eqs. (58) and (59). Equivalence with the model 2 is assumed and will be checked.

The above cases a–c will be later referred to as models 3a–3c.

5. Numerical comparative studies

Comparative studies will be performed carrying out simulation of the uniaxial compression test of a rock-type material using two cylindrical specimens with different particle size distribution. Different models, both with local size dependent and global uniform constitutive parameters, will be compared. Certain values of microscopic parameters will be assumed for the models with size dependent parameters and appropriate equivalent constant parameters for the model 3 will be calculated. Macroscopic behaviour obtained in numerical simulations will be studied by comparing stress–strain curves and macroscopic parameters: the Young's modulus, Poisson's ratio and compressive strength. Possible equivalence of the investigated models will be verified. The best method to evaluate global uniform constitutive parameters ensuring equivalence with a given model with local size dependent parameters will be identified.

The comparative studies for each specimen will be carried out according to the following plan:

1. Comparison of the models with local size dependent stiffness and strength parameters (models 1 and 2).
2. Comparison of each of the models with local size dependent parameters with appropriate models with global uniform parameters:
   (a) Comparison of the model 1 with the models 3a and 3b.
   (b) Comparison of the model 2 with the models 3a and 3c.

In the present work, the effect of the friction coefficient and damping will not be studied. All the cases will be calculated using the same value of the damping and friction. The value of the damping chosen for all the models will ensure quasi-static conditions.

5.1. Geometrical models

Two cylindrical specimens of diameter 23 mm and length 46 mm have been investigated. The first particle assembly has been generated using a special algorithm developed by Labra and Oñate (2009) and the second one has been obtained using a collective rearrangement algorithm with an imposed uniform particle size distribution, similar to the algorithm of Lubachevsky and Stillinger (1990). The specimens are characterized by different degree of geometric heterogeneity.

Table 4
Results of the UCS test for the specimen 1 and models with local evaluation of the parameters.

Effective mechanical property	Model 1	Model 2
Uniaxial compressive strength, σ_c (MPa)	299.91	241.38
Young's modulus, E (GPa)	20.32	20.13
Poisson's ratio, ν	0.16812	0.16801

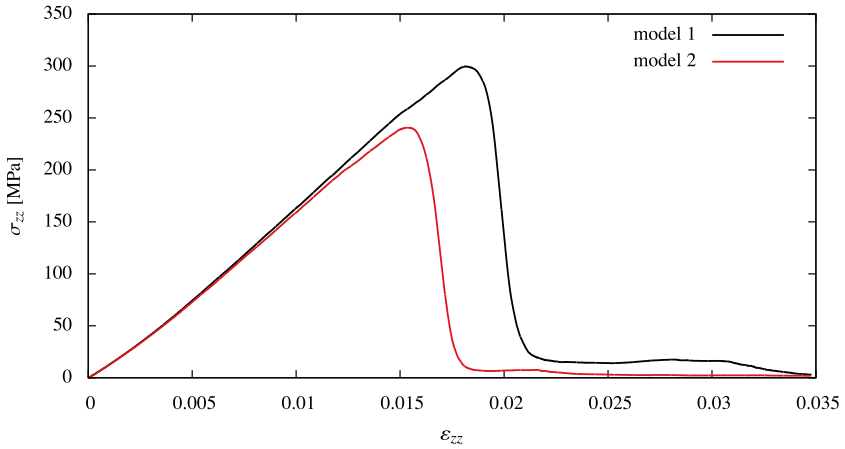

Fig. 12. Axial stress–strain curves for the models with local evaluation of the parameters – simulation results for the specimen 1.

5.1.1. Specimen 1

The first specimen, which will be later called the specimen 1, is more homogenous. It is formed by 10225 particles. The particle assembly is characterized by the particle size distribution shown in Fig. 5(a), the particle radii being in the range 0.3123–1.186 mm (the radius ratio $r_{max}/r_{min} = 3.8$). The porosity of the generated model is 23%.

The initial number of established contact bonds in the specimen 1 is 60809, with the coordination number $n_c = 11.89$. The histograms showing the distributions of the contact bond geometric parameters: of the arithmetic means of the radii of the contacting particle pairs, of the harmonic means of the radii of the contacting particle pairs and of the minimum radii of the contacting particle pairs are given in Fig. 5(b)–(d), respectively. It can be seen that

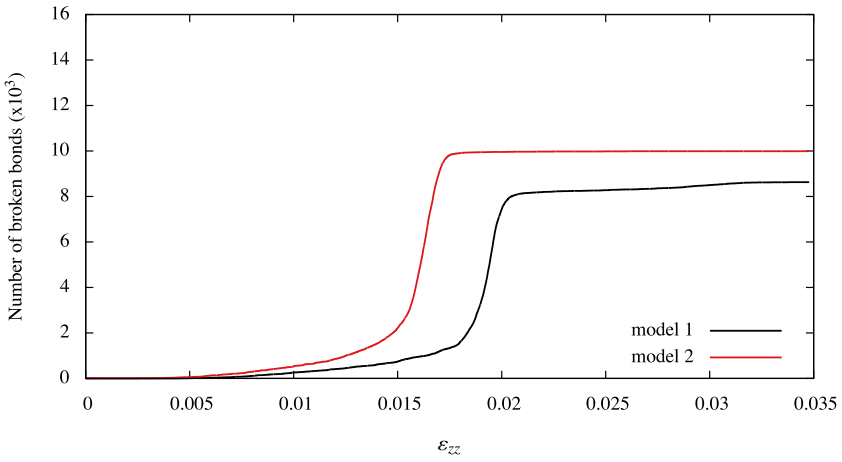

(a) Bonds broken due to shear

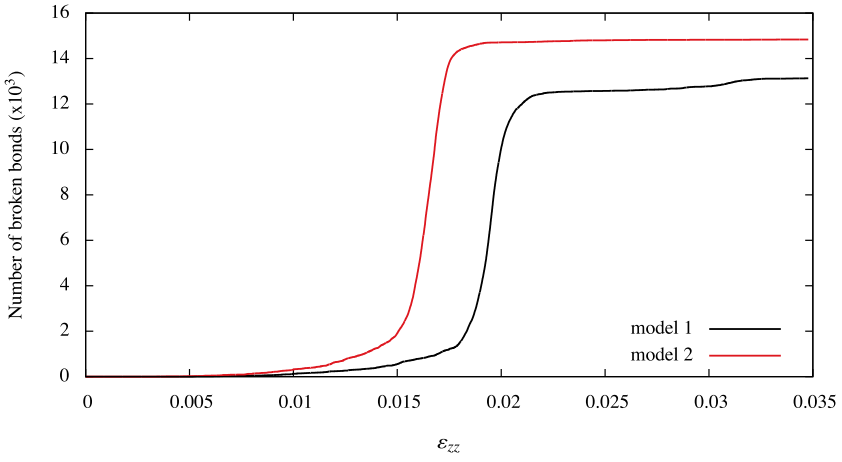

(b) Bonds broken due to tension

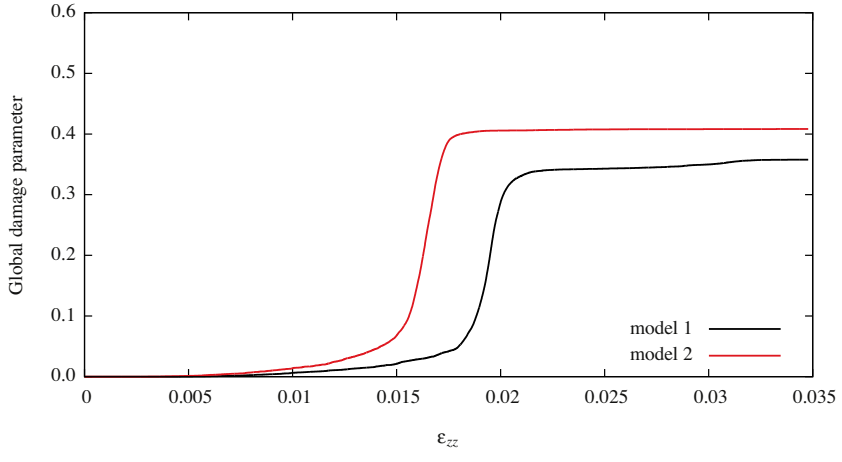

(c) Global damage parameter

Fig. 13. Damage evolution for the models with local evaluation of the parameters – simulation results for the specimen 1.

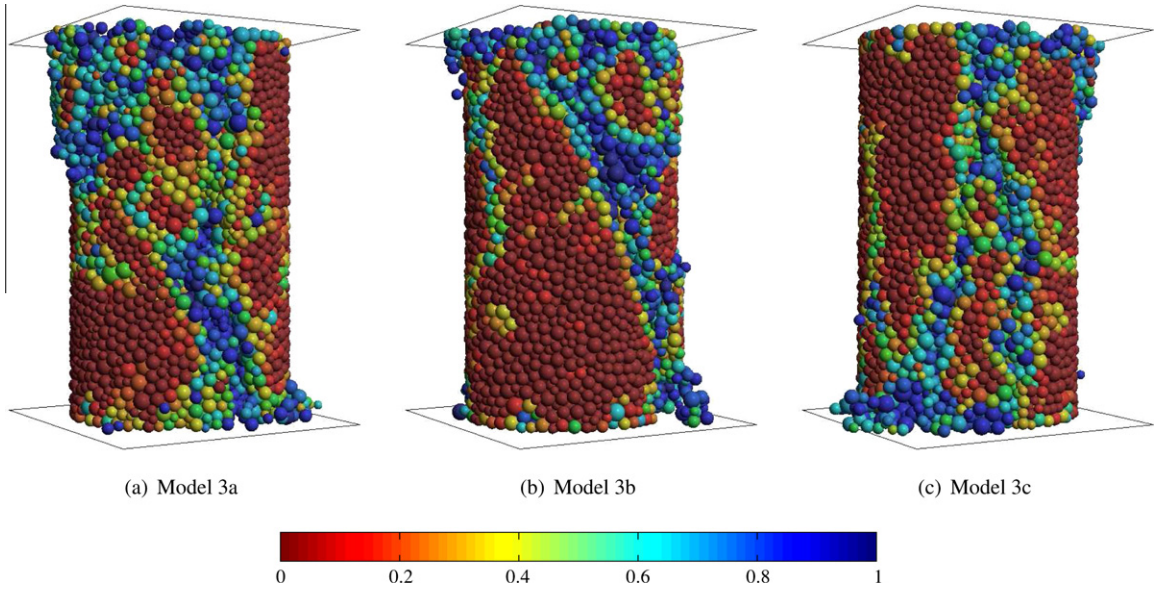

Fig. 14. Damage in the model with global uniform parameters – simulation results for the specimen 1.

the distributions shown in Fig. 5 are bounded, bell-shaped and nearly symmetrical. The statistics of the four distributions is summarized in Table A.1 in Appendix. The distribution of the particle radii in Fig. 5(a) can be treated as the parent distribution for the distributions in Fig. 5(b)–(d). In accordance with statistical rules the distributions in Fig. 5(b) and (c), obtained by averaging of randomly drawn samples from the parent distributions, are closer to the normal distribution in comparison with the parent distribution (Harnett, 1980; Kleijnen, 1987). The distribution of the minimum radii in Fig. 5(d) resembles the parent distribution.

Fig. 6 presents the polar distribution of the contact directions for the specimen 1 at the initial configuration. The histograms show fractions of contacts in assumed polar intervals. A uniform distribution of contacts, which can be seen, shows the isotropy of the particle assembly. The isotropy is also confirmed by the values of the diagonal components of the normalized fabric tensor: {0.33168, 0.33142, 0.33689}, cf. Bathurst and Rothenburg (1988), Madadi et al. (2004).

Fig. 7 presents distributions of the squares of the geometric parameters. It can be noticed the three distributions of the squares are slightly positively skewed. Table A.1 gives the statistics characterizing quantitatively the distributions of the squares. The squares of the characteristic local dimensions scale the strength of the contact bonds so their distributions can be treated as distributions of local strength in the model. The mean values of the distributions given in Table A.1 are equivalent to average parameters introduced in Section 4 which are used in the determination of equivalent contact stiffness and strength parameters.

Table 5
Results of the unconfined compressive strength test for the model 3 and specimen 1.

Effective mechanical property	Model 3a	Model 3b	Model 3c
Uniaxial compressive strength, σ_c (MPa)	269.89	292.59	232.14
Young's modulus, E (GPa)	18.90	19.31	19.16
Poisson's ratio, ν	0.16823	0.16830	0.16858

5.1.2. Specimen 2

The specimen 2 is modelled with 5868 particles. Particle size distribution is shown in Fig. 8(a). It can be regarded as approximately uniform. The particle assembly is more heterogenous than

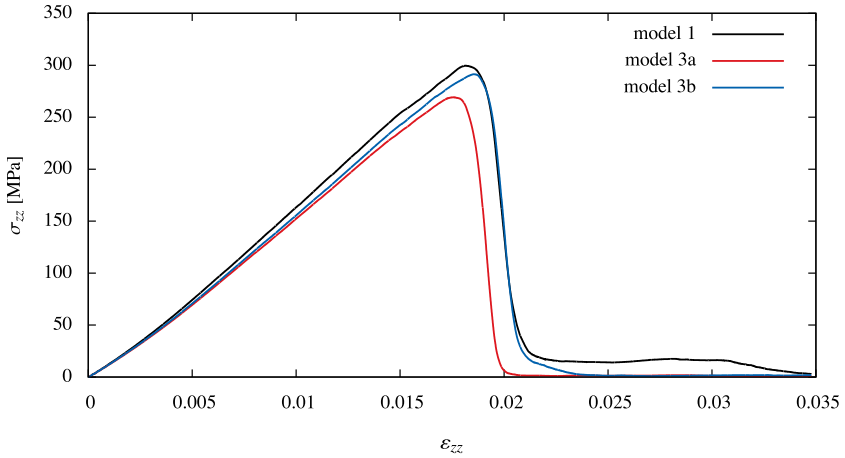

Fig. 15. Axial stress–strain curves – comparison of the model 1 with the models 3a and 3b for the specimen 1.

in the specimen 1. The particle radius range is 0.115–1.240 mm (the radius ratio $r_{max}/r_{min} = 10.8$) and the porosity is equal 27.53%.

The initial number of established contact bonds in the specimen 2 is 31431 with the coordination number $n_c = 10.713$. The distribution of contact bond geometric parameters: the arithmetic means of the radii of contacting particle pairs, the harmonic means of the radii of contacting particle pairs and the minimum radii of contacting particle pairs are shown in Fig. 8(b), (c) and (d), respectively. Statistical measures characterizing the distributions shown in Fig. 8 are given in Table A.2 along with the statistics for the distributions of the squares of the local size parameters shown in Fig. 9. The shapes of the distributions of the squares in Fig. 9 show significant asymmetry, which is confirmed by the statistical measures in Table A.2.

Isotropy of the particle assembly defining the specimen 2 is proved by the uniformity of the polar distribution of the contact directions given in Fig. 10. The diagonal components of the fabric tensor are the following: {0.33108, 0.33180, 0.33712}.

5.2. Model parameters

The model parameters assumed for the model 1 and 2 are presented in Table 1. The model parameters have been taken such that obtained macroscopic properties could characterize high strength brittle rocks. Using the parameters given in Tables 1 and A.1, and employing the methodology described in Section 4, the constitutive parameters for the three cases of the model 3 have been calculated for the specimen 1. Analogously, using the parameters given in Tables 1 and A.2, the constitutive parameters for the specimen 2 are calculated. The parameters for the specimens 1 and 2 are given in Tables 2 and 3, respectively.

The particle–platen interaction was modelled using the frictionless contact model with the penalty stiffness $K_n = 15$ MN/m. The compressive loading was introduced under constant velocity 0.2 m/s prescribed to the loading platens. The resulting axial strain rate is much higher than the loading strain rate in a quasi-static laboratory tests. However, the computational cost required in the discrete element simulations does not permit running simulations with real loading velocities. The loading rate sensitivity studies show that we can increase strain rate up to a certain level without changing much the mechanical response and failure process (Ma et al., 2011). With a proper damping coefficient, we have obtained a response which can be regarded as close to the quasi-static one. This is demonstrated below with the axial stress–strain curves which show no oscillations caused by dynamic effects.

5.3. Numerical results

Under an increasing load the damage in the specimen is developing progressively by breakage of bonds due to excessive shear or tensile forces until a complete failure is reached. The results of simulations are presented in the form of fractured specimens, axial stress–strain curves and plots showing evolution of damage. The specimens after failure are plotted with distribution of the damage parameter D, which is defined for each particle as:

$$D = 1 - \frac{b^t}{b^0} \tag{60}$$

where b^t is the number of bonded contacts of a given particle at time t, and b^0 – its initial number of bonded contacts.

The axial stress–strain curves are plotted taking the axial components of the average strain and stress tensors calculated for the whole specimen. The average strains have been estimated using the Bagi's equivalent continuum strain (Bagi, 1996; Durán et al., 2010). The stress is estimated using the averaging procedure of the micromechanical stress tensor (Kruyt and Rothenburg, 1996; Kruyt and Rothenburg, 2004). The slope of the stress–strain curves in the elastic range yields the Young's modulus, the peak point of these curves is taken as the compressive strength. The Poisson's ratio is determined in terms of the components of the average strain:

$$\nu = -\frac{0.5(\varepsilon_{xx} + \varepsilon_{yy})}{\varepsilon_{zz}} \tag{61}$$

where ε_{zz} is the axial strain, and $0.5(\varepsilon_{xx} + \varepsilon_{yy})$ is the average transverse strain.

5.4. Simulation results for specimen 1

The specimens after failure obtained in the simulations using the models 1 and 2 are presented in Fig. 11 with the distribution of the damage parameter. Failure pattern typical for brittle materials in the two models can be observed.

The stress–strain curves for the models 1 and 2 are plotted in Fig. 12 and the macroscopic properties are given in Table 4. The slope of the curves in Fig. 12 in the elastic range is almost identical, so the values of the Young's modulus calculated for both models are very similar, 20.32 GPa for the model 1 and 20.13 GPa for the model 2. This can be expected since the arithmetic and harmonic means used in the evaluation of contact stiffness in these models have very similar distributions (cf. Fig. 5(b) and (c)). The Young's modulus determined in the model 1 is slightly higher than that ob-

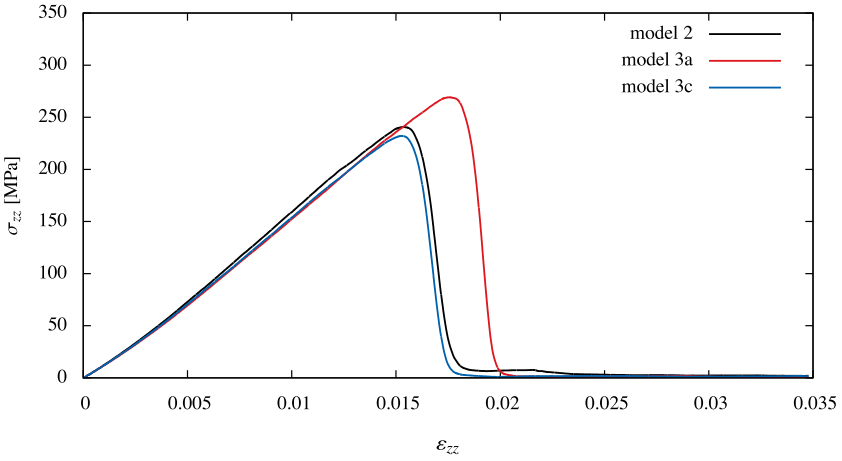

Fig. 16. Axial stress–strain curves – comparison of the model 2 with the models 3a and 3c for the specimen 1.

tained in the model 2. This is understandable since the arithmetic mean used in the model 1 to calculate the contact stiffness is always greater than the harmonic mean used in the model 2.

As it can be expected the failure load obtained using the model 2 is significantly lower than that obtained by the model 1. The microscopic strength in the model 2 is scaled by the minimum of the contacting particle radii which is the lower the arithmetic mean of the particle radii used for scaling in the model 2. Both models yield similar post-critical behaviour. The stress–strain curves in Fig. 12 drop immediately after the failure, which is typical for brittle materials. A similar softening rate is observed for both models.

The evolution of the damage in the specimens for both models is illustrated in Fig. 13 by the curves representing the number of

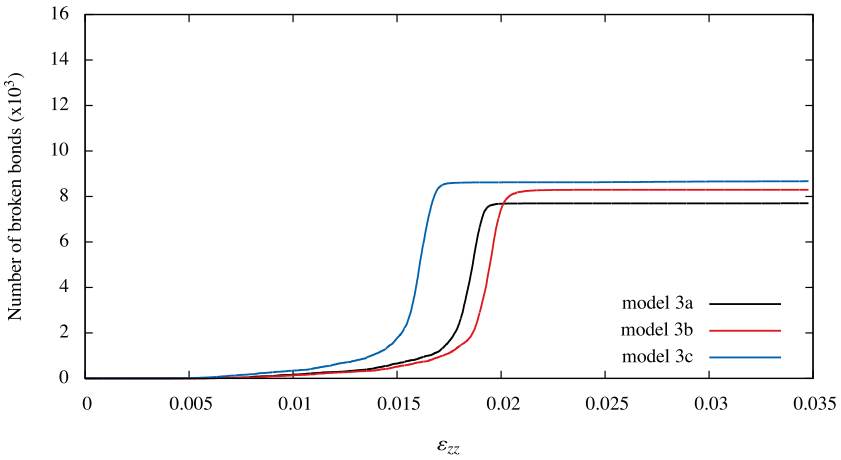

(a) Bonds broken due to shear

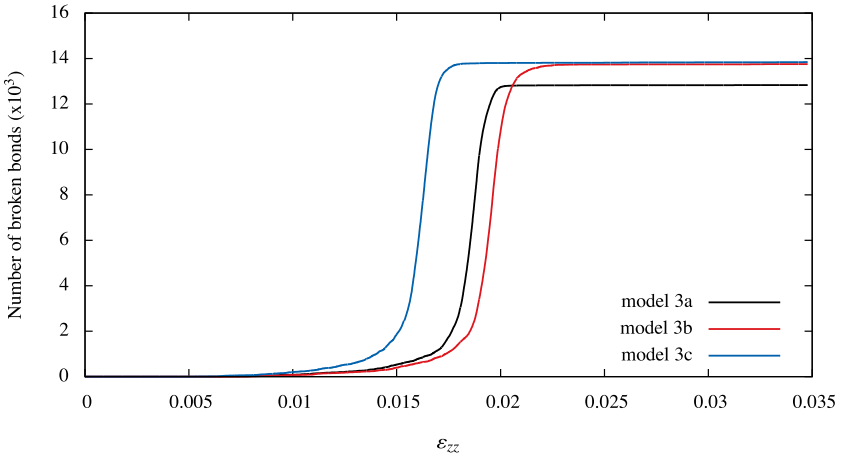

(b) Bonds broken due to tension

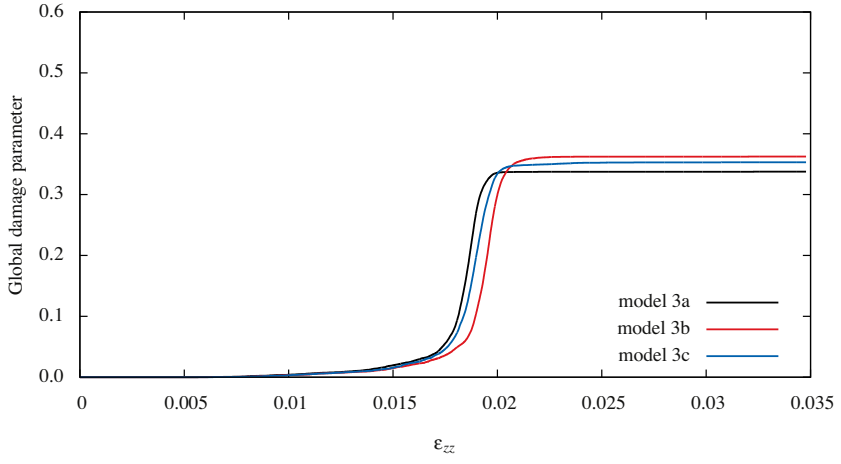

(c) Global damage parameter

Fig. 17. Damage evolution for the models with global uniform parameters – simulation results for the specimen 1.

bonds broken due to excessive tension and shear, and the global damage parameter as functions of the axial strain. The number of broken bonds in tension is slightly higher for both models. It is interesting to note that the model 2, which gives the lowest macroscopic strength, is characterized with the highest number of broken bonds. This can be attributed to the lowest microscopic strength/stiffness ratio in the model 2. This tendency will be manifested even more clearly for the more heterogenous specimen 2. The global damage parameter is calculated as the ratio of the number of broken bonds with respect to the initial number of cohesive bonds. This is equivalent to the average damage parameter defined in Eq. (60). This is a good indicator of damage distribution. The lower the global damage is, the more localized is the failure. It can be seen in Fig. 13(c) that the model 2 gives a slightly higher value of the damage parameter than the model 1. Difference in the damage distribution for these models is not appreciable in the failure patterns presented in Fig. 12, but the relationship between the global damage parameter and damage distribution will be clearly seen for the more heterogenous specimen 2.

A typical brittle failure is also predicted using the model with global uniform parameters. Fig. 14 shows the specimens after failure with the distribution of the damage parameter obtained for all the cases of the model 3. Quantitative results for all the cases of the model 3 are given in Table 5.

Figs. 15 and 16 show comparison of the stress–strain curves for the models with local size dependent contact parameters with the curves corresponding to respective cases of the model with global uniform parameters. Each of the two models with local size dependent constitutive parameters is compared to the model 3a whose parameters are evaluated according to the particle radius averages and one of the two other cases of the model 3 whose parameters are evaluated according to the respective averages of contact bond geometric parameters. Thus, the model 1 is compared with the models 3a and 3b in Fig. 15, and the model 2 is compared with the models 3a and 3c in Fig. 16.

Table 6
Results of the UCS test for the specimen 2 and models with local evaluation of the parameters.

Effective mechanical property	Model 1	Model 2
Uniaxial compressive strength, σ_c (MPa)	289.06	207.36
Young's modulus, E (GPa)	18.33	17.91
Poisson's ratio, ν	0.18565	0.18833

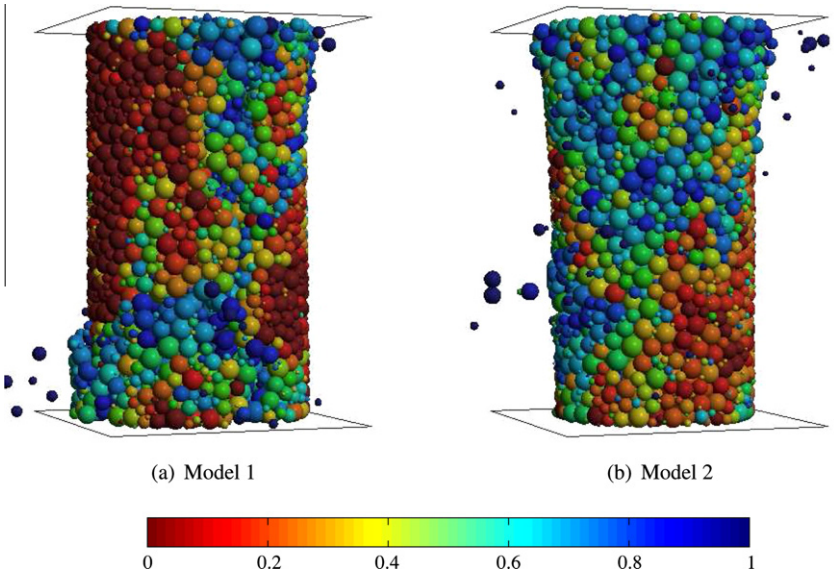

Fig. 18. Damage in the models with local evaluation of the parameters – simulation results for the specimen 2.

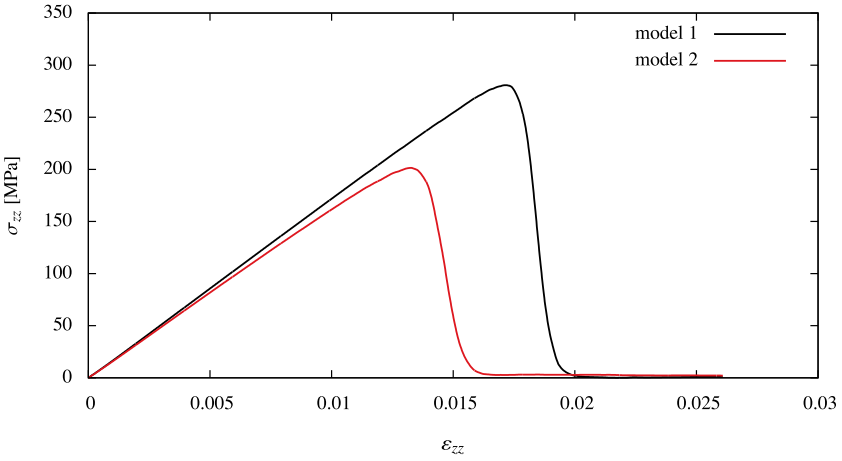

Fig. 19. Axial stress–strain curves for the models with local evaluation of the parameters – simulation results for the specimen 2.

Fig. 15 shows quite a good agreement between the stress–strain curves corresponding to the models 1 and 3b. The curve corresponding to the model 3a diverges slightly more from the curve corresponding to the model 1. This comparison shows that the evaluation of the parameters of the model 3 according to the averages of the arithmetic means of the contacting particles radii ensures practical equivalence of the models 3 and 1 for the specimen 1.

A very good agreement of the curves corresponding to the models 2 and 3c can be observed in Fig. 16. This indicates that the model 3 with uniform parameters calculated appropriately gives equivalent results to those produced by the model 2. The reasons

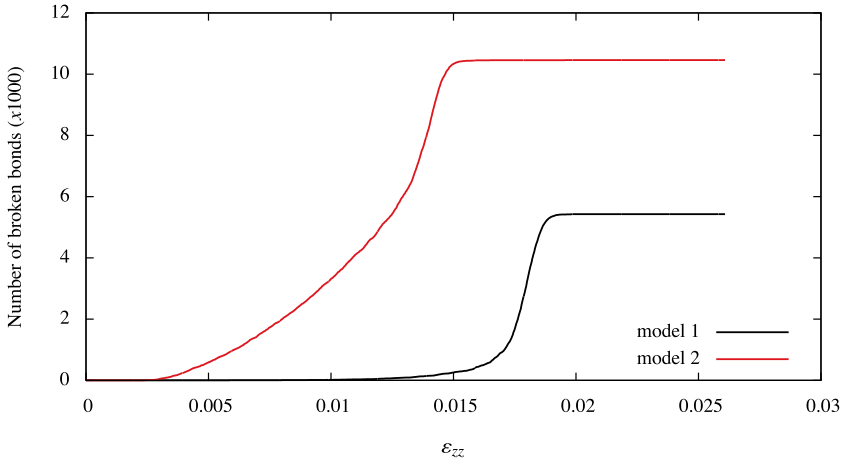

(a) Bonds broken due to shear

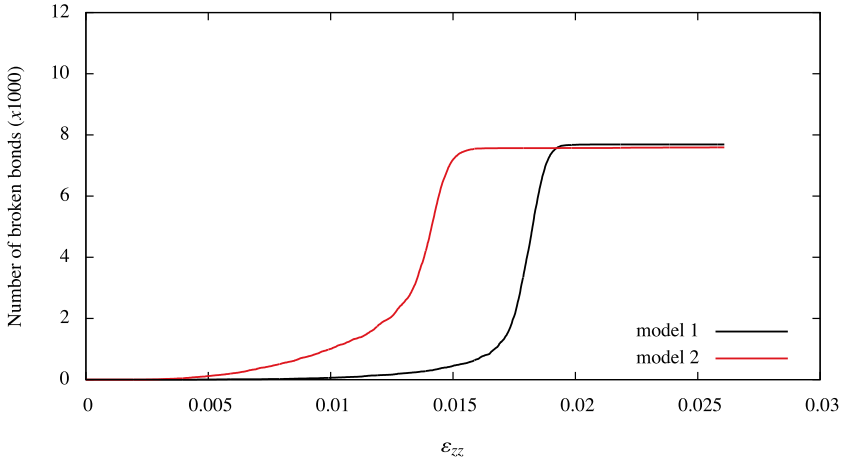

(b) Bonds broken due to tension

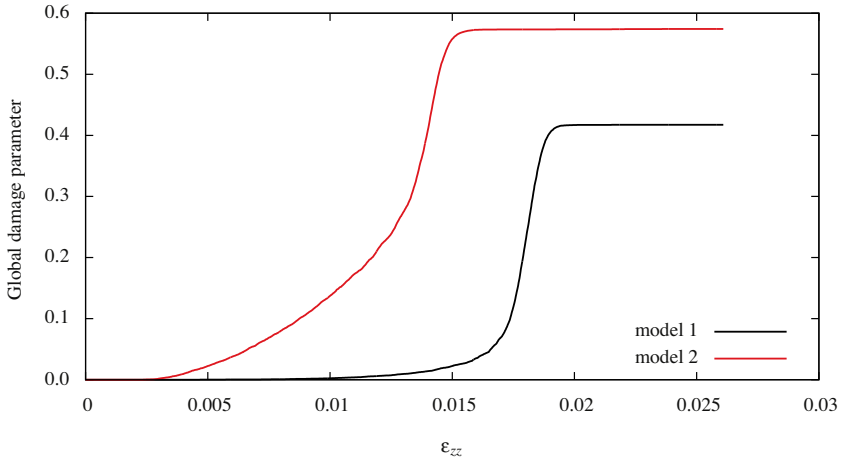

(c) Global damage parameter

Fig. 20. Damage evolution for the models with local evaluation of the parameters – simulation results for the specimen 2.

of an overestimation of the macroscopic strength by the model 3a, which can be seen in Fig. 16, are obvious. The minimum of the contacting particle radii gives much smaller bond strength than the strength estimated according to the average particle radius.

Fig. 17 illustrates the evolution of broken bonds in shear and tension, and the evolution of the global damage parameter for the specimen 1 with the 3 cases of the model with uniform constitutive parameters. The development of damage is similar for the 3 cases. In all the models the number of broken bonds in tension is slightly higher than in shear, which indicates a brittle type of failure. The final value of the global damage parameter is similar to the values obtained in the models with local evaluation of constitutive parameters. This indicates that the damage distribution should also be similar.

5.5. Simulation results for specimen 2

Fig. 18 shows failure modes obtained in the simulations using the specimen 2 with the models with size dependent parameters. The specimens after failure are presented with the distribution of the damage parameter D. It can be seen that the models 1 and 2 have produced different failure modes. The model 1 has given a more localized fracture while a distributed damage more typical for a ductile failure has been obtained with the model 2.

The axial stress–strain curves obtained for the models 1 and 2 are plotted in Fig. 19. The slope of the curves in the initial elastic range is similar. However, the slope of the curve corresponding to the model 2 starts to decrease at low load levels due to an early development of damage in the specimen. This can be attributed to the lower local strength of the bonds in the model 2. The lower bond strength also explains a lower failure load predicted by the model 2. Macroscopic properties determined in the simulations and given in Table 6 confirm observations made in the stress–strain plots.

The curves plotted in Fig. 20 confirm the development of damage in the model 2 from early stages of loading. It can also be observed that more bonds in the model 2 are broken in shear than in tension. Shear microfractures are typically associated with ductile rocks (Katz and Reches, 2004). This observation is in agreement with the failure mode presented in Fig. 18(b). The high value of the global damage parameter at specimen failure obtained using the model 2 suggests a significant damage distribution, which is again in agreement with Fig. 18(b). Comparing the plots for the specimens 1 and 2, in Figs. 13 and 20, it can be noticed that the geometric heterogeneity (the ratio r_{max}/r_{min}) has a smaller effect in case of the model 1. It can be understood that by taking the arithmetic mean of the particle radii to evaluate the bond strength (model 1) the heterogeneities are smoothed, while taking the smaller radius (model 2) allows the heterogeneities to manifest themselves fully.

The results of the simulations using the specimen 2 with different sets of equivalent parameters are shown in Fig. 21 in the form of the specimens after failure with damage distribution. It can be seen that a typical brittle failure characterized by localized fracture has been predicted by the model with uniform constitutive parameters. Macroscopic properties calculated for all the cases of the model 3 are summarized in Table 7.

Figs. 22 and 23 show comparison of the axial stress–strain curves for the models with the local size dependent constitutive parameters and respective cases of the model 3 with the global uniform constitutive parameters. Similarly as for the specimen 1, both models with the local size dependent contact parameters are compared with the model 3a, whose parameters are evaluated according to the particle radius averages and one of the two other cases of the model 3, whose parameters are evaluated according to the respective averages of contact bond geometric parameters. Thus, the model 1 is compared with the models 3a and 3b in Fig. 22, and the model 2 is compared with the models 3a and 3c in Fig. 23. Noticeable differences between the compared curves can be seen, which means that for the more heterogenous specimen the models produce different responses. The model 3a gives a bigger difference in response with respect to the models 1 and 2, which means that evaluation of global uniform parameters for the model 3 using the mean particle radius does not ensure equivalent properties to those of the models 1 or 2. The difference is

Table 7
Results of the unconfined compressive strength test for the model 3 and specimen 2.

Effective mechanical property	Model 3a	Model 3b	Model 3c
Uniaxial compressive strength, σ_c (MPa)	193.85	313.41	187.06
Young's modulus, E (GPa)	14.08	17.42	16.45
Poisson's ratio, ν	0.18580	0.18526	0.18573

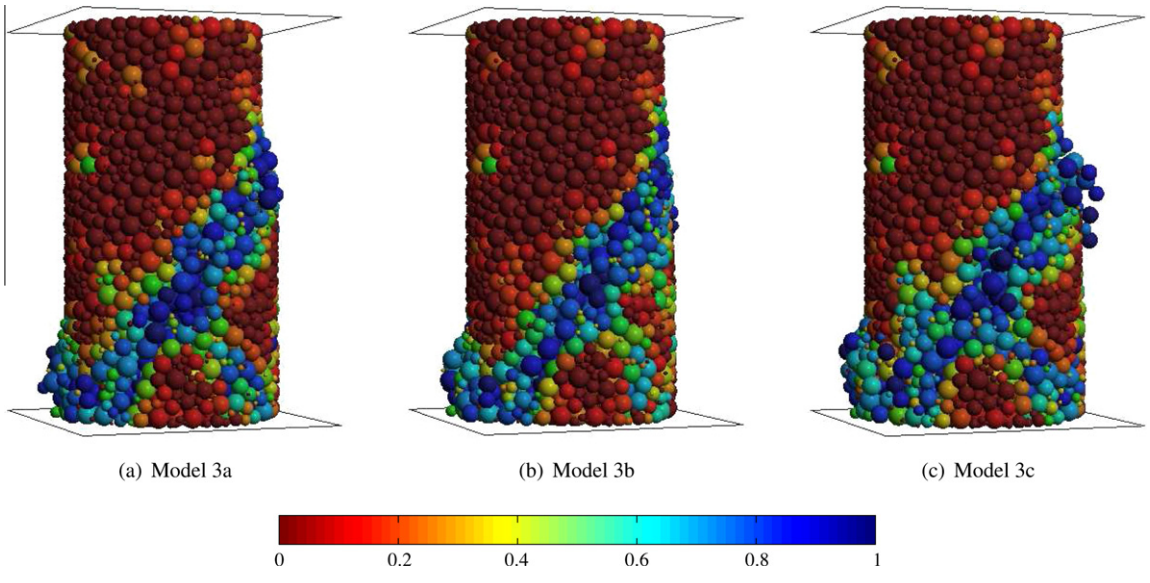

Fig. 21. Damage in the model with global uniform parameters – simulation results for the specimen 2.

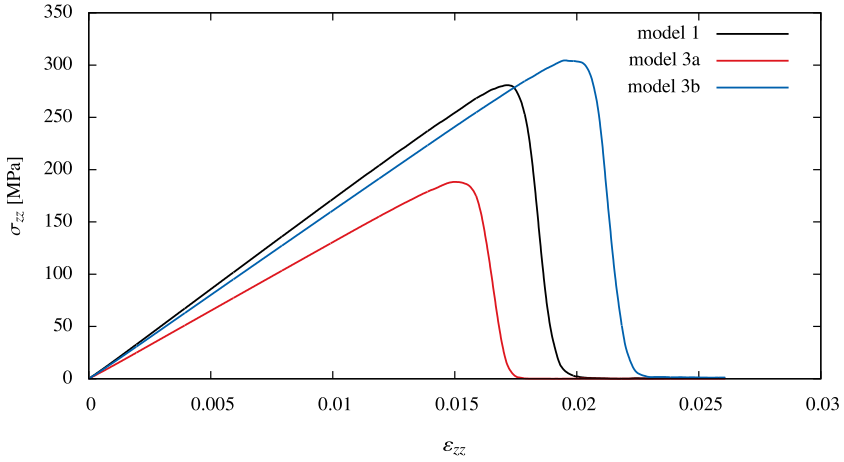

Fig. 22. Axial stress–strain curves – comparison of the model 1 with the models 3a and 3b for the specimen 2.

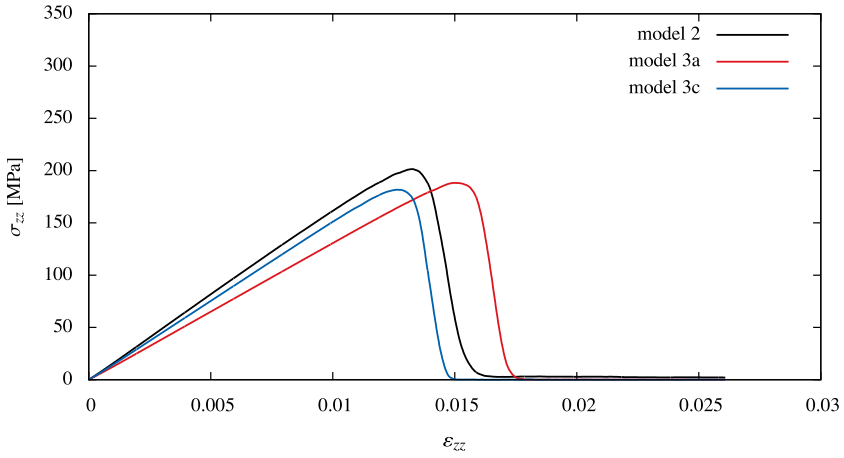

Fig. 23. Axial stress–strain curves – comparison of the model 2 with the models 3a and 3c for the specimen 2.

smaller in case of comparison of the model with local evaluation of constitutive parameters and the models, whose parameters are evaluated according to the respective averages of contact bond geometric parameters, namely between the models 1 and 3b, and between the models 2 and 3c. This confirms that this method of evaluation of the global uniform constitutive parameters ensures a better equivalence with the respective models using local evaluation of constitutive parameters.

The curves illustrating the damage evolution plotted in Fig. 24 confirm a brittle and localized failure of the specimen 2 with the models employing uniform constitutive parameters. Tension dominates over shear as a failure mechanism, which is associated with a brittle failure. A small value of the global damage parameter indicates a localized fracture.

6. Conclusions

The results of the comparative studies presented above provide interesting observations on the effect of the evaluation method of the contact parameters in the discrete element method. Comparison of qualitative and quantitative results shows some similarities and differences.

The results are quite similar for the more homogenous specimen (specimen 1). The two models with local evaluation of the constitutive parameters (models 1 and 2) predict very similar elastic properties, which can be explained by a small difference in this specimen between the arithmetic and harmonic means, the geometric scaling parameters used in these models to calculate the contact stiffness. Nevertheless, even for this specimen, the relationship between the scaling parameters are reflected correctly in the values of macroscopic properties. The model with the contact stiffness scaled according to the arithmetic mean of the contacting particle radii (model 1) yields slightly higher values of the Young's modulus than the model with the contact stiffness scaled according to the harmonic mean (model 2), which is understandable having in mind that the arithmetic mean is always greater than the harmonic mean. The difference in the macroscopic stiffness manifests itself more clearly in the specimen with a higher radius ratio.

The compressive strength predicted by the model 2 for both specimens is considerably smaller than that obtained using the model 1. This could be expected, since the minimum radius of the contact pair used as the scaling factor to determine the contact bond strength in the model 2 is smaller than the arithmetic mean of the radii of the contacting particle pair which is used to scale the contact strength in the models 1.

It can be observed that damage in the specimens with the model 2 is initiated at lower loading levels than in the specimens with the model 1. This can be explained by a lower bond strength in the

model 2. This is also the reason, why the damage development is more rapid and the damage is more distributed in the model 2 than in the model 1. This is especially visible in the more heterogenous specimen. The evolution of damage shows that the failure predicted by the model 2 is characterized by a greater number of broken bonds than in the case of the model 1. This indicates a more distributed damage which is confirmed by the images of failed specimens.

In most cases, the failure of the specimens predicted by the analysis can be regarded as brittle, only in case of the specimen 2 with the model 2 a distributed damage typical for a ductile failure is obtained. The ductile character of the failure is associated with shear-dominant failure at the micromechanical level. The effect of the geometric heterogeneity (the ratio r_{max}/r_{min}) on the failure mechanism is especially appreciable for the model 2. It can be understood that the evaluation of the strength parameters in the

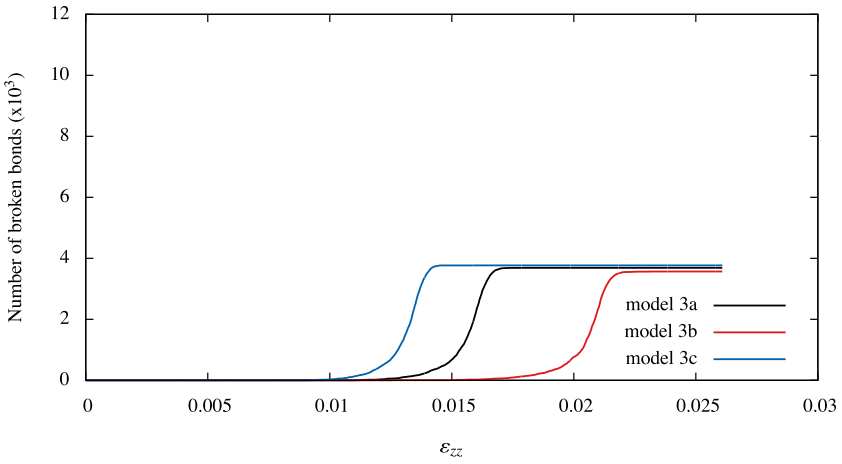

(a) Bonds broken due to shear

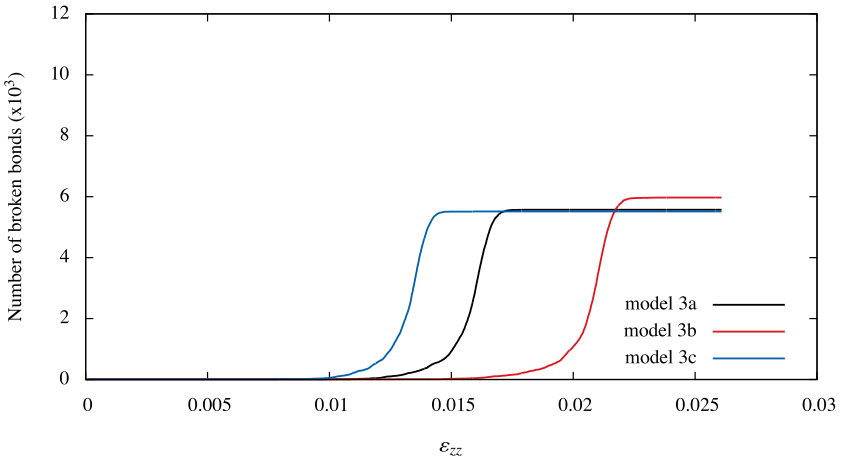

(b) Bonds broken due to tension

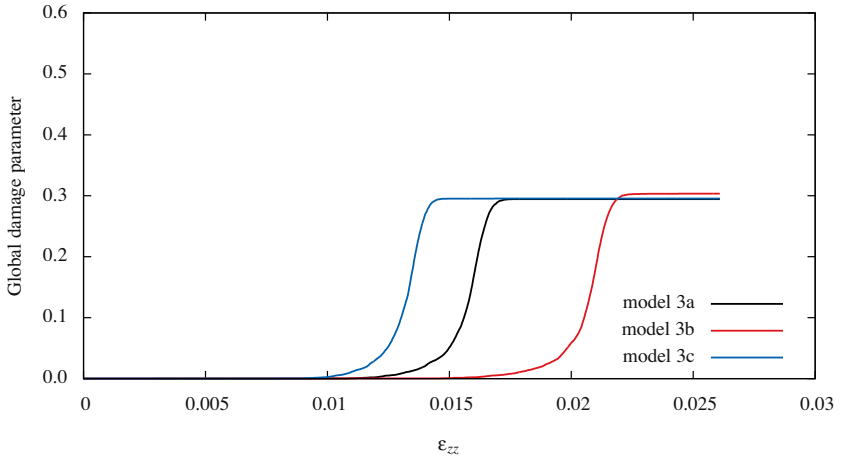

(c) Global damage parameter

Fig. 24. Damage evolution for the models with global uniform parameters – simulation results for the specimen 2.

Table A.1
Statistics summary of the distributions of the particle radii and contact bonds geometric parameters for the specimen 1.

Description	r	$\bar{r}$	$\tilde{r}$	r_m	r^2	$\bar{r}^2$	r_m^2
Mean	0.6759350	0.7032214	0.6909727	0.6291815	0.4750058	0.5045808	0.4080978
Median	0.6714439	0.7001103	0.6882989	0.6290655	0.4508369	0.4901544	0.3957234
Std. deviation	0.1346085	0.1003028	0.1019053	0.1105832	0.1876938	0.1435643	0.1416917
Skewness	0.2241149	0.1806703	0.1839703	0.1245392	0.7833898	0.5884414	0.6298497
Kurtosis	−0.0612598	−0.0532155	−0.0599418	−0.0681768	0.7989896	0.4346718	0.5643835
Minimum	0.3122622	0.3672905	0.3632630	0.3122622	0.0975077	0.1349023	0.0975077
Maximum	1.1861220	1.1141005	1.1136308	1.0926130	1.4068854	1.2412199	1.1938032

Table A.2
Statistics summary of the distributions of the particle radii and contact bonds geometric parameters for the specimen 2.

Description	r	$\bar{r}$	$\tilde{r}$	r_m	r^2	$\bar{r}^2$	r_m^2
Mean	0.6993391	0.8338194	0.7664190	0.6556167	0.5948130	0.7374067	0.5090438
Median	0.7023354	0.8425944	0.7868309	0.6540944	0.4932754	0.7099654	0.4278394
Std. deviation	0.3252012	0.2053124	0.2536868	0.2814481	0.4625653	0.3329340	0.3789057
Skewness	−0.0103777	−0.3161015	−0.2104510	0.0276287	0.4682580	0.1937488	0.5942279
Kurtosis	−1.2784650	−0.4576297	−0.9823256	−1.0820407	−1.1066860	−0.8110736	−0.7152502
Minimum	0.1151885	0.1695048	0.1584173	0.1151884	0.0132684	0.0287318	0.0132683
Maximum	1.2399406	1.2358476	1.2358465	1.2346827	1.5374527	1.5273192	1.5244413

model 2 increases heterogeneous nature of the model, while the approach in the model 2 consisting in scaling of the bond strength according to the particle radii leads to smoothing of heterogeneities.

Similarly we can explain the failure mechanism observed in the specimens with the all the cases of the model 3. Despite the geometric heterogeneity, the uniform constitutive parameters result in localized brittle-like fractures. The localized nature of the failure predicted by the models 3 is confirmed by a lower level of global damage parameter evaluated for the whole specimen. The difference of the failure mode obtained with the models 3 with respect to other models is especially apparent for the specimen 2. The failure pattern predicted by the models 3 for the specimen 1 is similar to those predicted by the models with local evaluation of constitutive parameters.

For the specimen with a relatively low geometric heterogeneity, the model with global uniform constitutive parameters can give results similar to those produced by the models with locally evaluated size dependent contact parameters. In order to get equivalent quantitative results using these two approaches, it is desirable to determine equivalent global uniform parameters using the distributions of the appropriate geometric parameters employed as scaling factors in respective models with local size dependent constitutive parameters. The parameters evaluated in this way give a better agreement than the parameters evaluated according to the average particle size in the discrete element assembly. The latter approach does not take into account actual geometric parameters used in the evaluation of contact parameters.

Appendix A. Statistics summary

Tables A.1 and A.2.

References

Agnolin, I., Roux, J.-N., 2008. On the elastic moduli of three-dimensional assemblies of spheres: characterization and modeling of fluctuations in the particle displacement and rotation. International Journal of Solids and Structures 45, 1101–1123.

Antonellini, M., Pollard, D., 1995. Distinct element modeling of deformation bands in sandstone. Journal of Structural Geology 17 (8), 1165–1182.

Bagi, K., 1996. Stress and strain in granular assemblies. Mechanics of Materials 22 (3), 165–177.

Bathurst, R., Rothenburg, L., 1988. Micromechanical aspects of isotropic granular assemblies with linear contact interactions. Journal of Applied Mechanics, ASME 55 (1), 17–23.

Bažant, Z., Pang, S., Vorechovsky, M., Novak, D., Pukl, R., 2004. Statistical size effect in quasibrittle materials: computation and extreme value theory. In: Li, V.C., Leung, K., Willam, K., Billington, S. (Eds.), Fracture Mechanics of Concrete Structures. IA-FraMCoS, pp. 189–196.

Blair, S., Cook, N., 1998. Analysis of compressive fracture in rock using statistical techniques: Part II. Effect of microscale heterogeneity on macroscopic deformation. International Journal of Rock Mechanics Mining Sciences 35, 849–861.

Boutt, D., McPherson, B., 2002. The role of particle packing in modeling rock mechanical behavior using discrete elements. In: Cook, B., Jensen, R. (Eds.), Discrete Element Methods, 3rd International Conference. ASCE, New Mexico.

Cambou, B., Chaze, M., Dedecker, F., 2000. Change of scale in granular materials. European Journal Mechanics A Solids 19, 999–1014.

Chang, C., Hicher, P.-Y., 2005. An elasto-plastic model for granular materials with microstructural consideration. International Journal of Solids and Structures 42, 4258–4277.

Choi, S., 1992. Application of the distinct element method for rock mechanics problems. Engineering Computations 9, 225–233.

CIMNE, 2010. Dempack, explicit nonlinear dynamic analysis by the finite and discrete element method. web:<www.cimne.upc.edu/dempack>.

Cundall, P., Strack, O., 1979. A discrete numerical method for granular assemblies. Geotechnique 29, 47–65.

Cundall, P.A., 1988a. Computer simulations of dense sphere assemblies. In: Satake, M., Jenkins, J. (Eds.), Studies Applied Mechanics, pp. 113–123.

Cundall, P.A., 1988b. Formulation of a three dimensional distinct element model – Part I. A scheme to detect and represent contacts in a system of many polyhedral blocks. International Journal of Rock Mechanics Mining Sciences and Geomechanics Abstracts 25 (3), 107–116.

D'Addetta, G., Kun, F., Ramm, E., 2002. On the application of a discrete model to the fracture process of cohesive granular materials. Granular Matter 4, 77–90.

Donze, F., Richefeu, F., Magnier, S., 2009. Advances in discrete element method applied to soil, rock and concrete mechanics. Electronic Journal of Geotechology Engineering 08, 1–44, Special volume, Bouquet.

Durán, O., Kruyt, N., Luding, S., 2010. Analysis of three-dimensional micro-mechanical strain formulations for granular materials: evaluation of accuracy. International Journal of Solids and Structures 47 (2), 251–260.

Fakhimi, A., Villegas, T., 2007. Application of dimensional analysis in calibration of a discrete element model for rock deformation and fracture. Rock Mechanics and Rock Engineering 40 (2), 193–211.

Harnett, D.L., 1980. Introductory Statistical Analysis. Addison-Wesley.

Hentz, S., Daudeville, L., Donze, F., 2004. Identification and validation of a discrete element model for concrete. Journal of Engineering Mechanics 130, 709–719.

Herrmann, H., Roux, S., 1990. Modelization of fracture in disordered systems. In: Herrmann, H., Roux, S. (Eds.), Statistical Models for the Fracture of Disordered Media. Elsevier, pp. 159–188.

Hsieh, Y.-M., Li, H.-H., Huang, T.-H., Jeng, F.-S., 2008. Interpretations on how the macroscopic mechanical behavior of sandstone affected by microscopic properties – revealed by bonded-particle model. Engineering Geology, 1–10.

Huang, H. 1999. Discrete element modeling of tool-rock interaction. Ph.D. Thesis, December, University of Minnesota.

Huang, H., Detournay, E., 2008. Intrinsic length scales in tool-rock interaction. International Journal of Geomechanics 8 (1), 39–44.

Katz, O., Reches, Z., 2004. Microfracturing, damage, and failure of brittle granites. Journal of Geophysical Research 109, 1206–1218.
Kleijnen, J., 1987. Statistical Tools for Simulation Practitioners. Marcel Dekker Inc.
Kruggel-Emden, H., Wirtza, S., Scherera, V., 2008. A study on tangential force laws applicable to the discrete element method (DEM) for materials with viscoelastic or plastic behavior. Chemical Engineering Science 63 (6), 1523–1541.
Kruyt, N., Rothenburg, L., 2004. Kinematic and static assumptions for homogenization in micromechanics of granular materials. Mechanics of Materials 36 (12), 1157–1173.
Kruyt, N.P., Rothenburg, L., 1996. Micromechanical definition of the strain tensor for granular materials. Journal of Applied Mechanics 118, 706–711.
Labra, C., Oñate, E., 2009. High-density sphere packing for discrete element method simulations. Communications in Numerical Methods in Engineering 25 (7), 837–849.
Liao, C.-L., Chan, T.-C., 1997. A generalized constitutive relation for a randomly packed particle assembly. Computers and Geomechnics 20 (3-4), 345–363.
Liao, C.-L., Chang, T.-P., Young, D.-H., 1997. Stress–strain relationship for granular materials based on the hypothesis of best fit. International Journal of Solids and Structures 34 (31/32), 4087–4100.
Lubachevsky, B., Stillinger, F., 1990. Geometrik properties of random disk packings. Journal of Statistical Physics 60, 561–583.
Luding, S., 2008. Cohesive, frictional powders: contact models for tension. Granular Matter 10 (4), 235–246.
Ma, G., Wang, X., Ren, F., 2011. Numerical simulation of compressive failure of heterogeneous rock-like materials using SPH method. International Journal of Rock Mechanics and Mining Sciences 48, 353–363.
Madadi, M., Tsoungui, O., Lätzel, M., Luding, S., 2004. On the fabric tensor of polydisperse granular materials in 2D. International Journal of Solids and Structures 41 (9–10), 2563–2580.
Munkholm, L., Perfect, E., 2005. Brittle fracture of soil aggregates: Weibull models and methods of parameter estimation. Soil Science Society America Journal 69, 1565–1571.
Ng, T.-T., 2006. Input parameters of discrete element methods. Journal of Engineering Mechanics 132 (7), 723–729.
Oñate, E., Rojek, J., 2004. Combination of discrete element and finite element methods for dynamic analysis of geomechanics problems. Computer Methods in Applied Mechanics and Engineering 193 (27–29), 3087–3128.
PFC^{3D}, 2006. Particle flow code in 3D, theory and background manual. Itasca, Minneapolis, MN, USA.
Potyondy, D., Cundall, P., 2004. A bonded-particle model for rock. International Journal of Rock Mechanics and Mining Sciences 41 (8), 1329–1364, Rock Mechanics Results from the Underground Research Laboratory, Canada.
Price, H., Martin III, R., Boyd, P., Boitnott, G. 1994. Mechanical and bulk properties of intact rock collected in the laboratory in support of the yucca mountain site characterization project. Technical Report SAND94-2243C, Sandia National Laboratories Data Report.
Rojek, J., Oñate, E. 2004. Unified DEM/FEM approach to geomechanics problems. In: Proceedings of Computational Mechanics WCCM VI in conjunction with APCOM04, Beijing, China, September 5–10.
Rojek, J., Oñate, E., Kargl, H., Labra, C., Akerman, J., Restner, U., Lammer, E., Zarate, F., 2008. Prediction of wear of roadheader picks using numerical simulations. Geomechanik und Tunnelbau 1 (1), 47–54.
Rojek, J., Oñate, E., Labra, C., Kargl, H., 2011. Discrete element simulation of rock cutting. International Journal of Rock Mechanics and Mining Sciences 48 (6), 996–1010.
Rojek, J., Oñate, E., Zarate, F., Miquel, J. 2001. Modelling of rock, soil and granular materials using spherical elements. In: 2nd European Conference on Computational Mechanics ECCM-2001, Cracow, Poland.
Tavarez, F.A., Plesha, M.E., 2007. Discrete element method for modelling solid and particulate materials. International Journal for Numerical Methods in Engineering 70 (4), 379–404.
Voivret, C., Delenne, J.-Y., Radjai, F., Youssoufi, M.E. 2009. Force transmission in highly polydisperse granular media. In: AIP Conference Proceedings, vol. 1145, pp. 297–300.
Wang, Y., Tonon, F., 2009. Modeling Lac du Bonnet granite using a discrete element model. International Journal of Rock Mechanics and Mining Sciences 46, 1124–1135.